Chapter 8

Compact Metamaterials Induced Circuits and Functional Devices

He-Xiu Xu, Guang-Ming Wang, Tong Cai,
Qing Peng and Ya Qiang Zhuang

Additional information is available at the end of the chapter

http://dx.doi.org/10.5772/65603

Abstract

In recent years, we have witnessed a rapid expansion of using metamaterials to manipulate light or electromagnetic (EM) wave in a subwavelength scale. Specially, metamaterials have a strict limitation on element dimension from effective medium theory with respect to photonic crystals and other planar structures such as frequency selective surface (FSS). In this chapter, we review our effort in exploring physics and working mechanisms for element miniaturization along with the resulting effects on element EM response. Based on these results, we afford some guidelines on how to design and employ these compact meta-atoms in engineering functional devices with high performances. We found that some specific types of planar fractal or meandered structures are particularly suitable to achieve element miniaturization. In what follows, we review our effort in Section 1 to explore novel theory and hybrid method in designing broadband and dual band planar devices. By using single or double such compact composite right-/left-handed (CRLH) atom, we show that many microwave/RF circuits, i.e., balun, rat-race coupler, power divider and diplexer, can be further reduced while without inducing much transmission loss from two perspectives of lumped and distributed CRLH TLs. In Section 2, we show that a more compact LH atom can be engineered by combining a fractal ring and a meandered thin line. Numerical and experimental results demonstrate that a subwavelength focusing is achieved in terms of smooth outgoing field and higher imaging resolution. Section 3 is devoted to a clocking device from the new concept of superscatterer illusions. To realize the required material parameters, we propose a new mechanism by combining both electric and magnetic particles in a composite meta-atom. Such deep subwavelength particles enable exact manipulation of material parameters and thus facilitate desirable illusion performances of a proof-of-concept sample constructed by 6408 gradually varying meta-atoms. Finally, we summarize our results in the last section.

Keywords: metamaterials, fractal, electrically small, effective medium, broadband, CRLH TL, microwave/RF circuits, super lens, cloaking

1. Miniaturized CRLH atoms for compact microwave/RF circuits

Compact metamaterial element exhibits versatile features and merits over its conventional counterparts. One of the most important and direct features is that it enables more compact microwave/RF circuits. In this section, we will show this first benefit through a set of compact metamaterial transmission lines (TL), i.e., compact composite right/left-handed (CRLH) TLs. For a comprehensive study, two types of compact CRLH TLs, namely, lumped and distributed CRLH TLs, are investigated according to the realization manner. Of particular relevance and importance is the established design guideline, which paves the way for any microwave and millimeter wave integrated circuits and devices with high performances.

1.1. CAD design method for fractal lumped CRLH TL

To begin with, we first derive a general design mythology for the design of any compact CRLH element with fractal or meandered sections. **Figure 1** depicts the CAD design flowchart of such CRLH TLs. For analysis convenience, the general circuit model (CM) of any CRLH TL is reproduced in **Figure 1(a)**. The CRLH TL, with characteristic impedance of Z_c at angular frequency ω and element number of N, consists of left-handed (LH) contribution associated with L_L, $C_{L,}$ and right-handed (RH) part with L_R, C_R. This CM topology can be easily converted to T-type circuit with $L_R/2$ and $2C_L$. In practical realization, the RH part is designed by microstrip line (ML) in meandered topology, whereas the chip components based on surface mount technology (SMT) are utilized to realize the LH part of CRLH atom. As such, the circuit

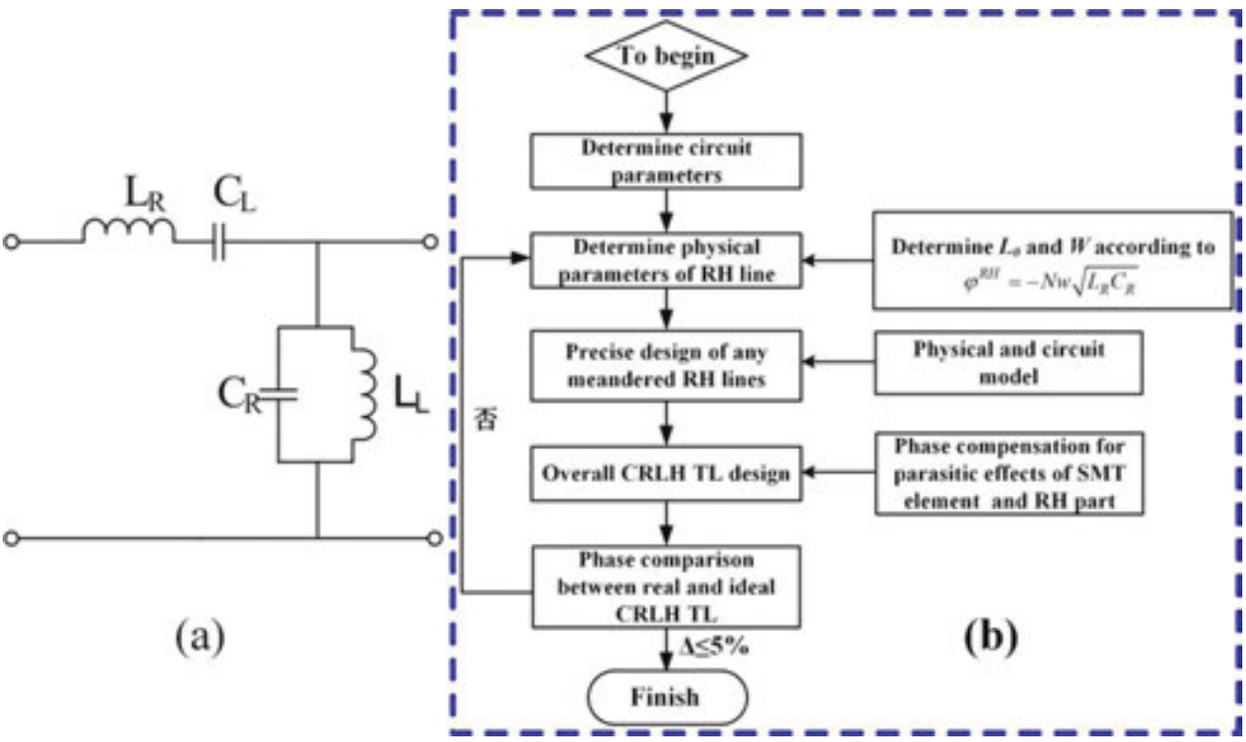

Figure 1. (a) Circuit topology and (b) CAD design flowchart of fractal or meandered CRLH TL.

miniaturization and weakened susceptibility of meandering effects on the characteristic impedance are simultaneously engineered by taking advantages of both space-filling fractals/meanderings and CRLH technology. The design procedures, which mainly concentrate on phase, are described as follows.

(1) Determine and derive the circuit parameters of any CRLH TL according to the required phase response at operation frequency f_0 based on circuit theory. Here, the desired phase response is synthesized based on the realized functionality.

(2) Given the computed values of LR and CR, the required electrical length of straight RH line (ML) for CRLH TL is determined by

$$\varphi(\omega_0) = -N\omega_0\sqrt{L_R C_R} \tag{1}$$

Therefore, the physical length L_0 and width w are directly obtained referring to the $\varphi(\omega_0)$ and characteristic impedance in circuit simulation package of Ansoft Serenade.

(3) Design any fractal ML with specified phase shift. Since many chamfered bends are generated in iterative meandered process, the nonnegligible discontinuity reactance results in phase-shifting effect of RH line which should be properly evaluated and compensated. Here, a phase-equalizing method is developed. A slight physical length Δb corresponding to the phase shift generated by each bend is applied to model the effect. Consequently, the L_0 should be added by Δb per bend for compensation. The value of Δb in millimeter is determined by [1]:

$$\Delta b = \frac{19.2\pi h}{\sqrt{\varepsilon_{eff}} Z_C}\left[2-\left(f_0 h/0.4Z_C\right)^2\right] \tag{2}$$

Here, ε_{eff}, h are effective dielectric constant and height of the substrate in millimeter, respectively.

(4) Design the overall CRLH TL by taking into account the parasitic inductances and capacitances of SMT elements and soldering pad. This can be implemented by a close-loop precise optimization through dynamically comparing the phase response of real and ideal CRLH TLs. Here, the parasitic effects are evaluated through a direct comparison of measured transmission response of MLs with and without soldered SMT elements.

1.2. Broadband and dual band balun

1.2.1. Broadband balun using fully artificial fractal-shaped CRLH TL

In this subsection, a compact balun with bandwidth enhancement is realized based on the design methodology established in Section 1.1.

Balun, a three-port network, was commonly used to transfer the input unbalanced signal to two output balanced ones with 180° phase difference. It has been extensively studied for active amplifiers, balanced mixers, passive filter [2] and even antennas [3]. Several types of baluns are available among the open literature, such as the Marchand balun [4–6], power-divider balun [7, 8], branch-line balun [9] and metamaterial balun [10]. Highly integrated

circuits with stable communication quality strongly require wideband and miniaturized RF/microwave devices. In this regard, several strategies have been proposed for miniaturization, e.g., by integrating coupled transmission line (TL) [4], using low temperature cofired ceramic technique [5] or fractal/meandered branches [9–11]. Although baluns achieved significant miniaturization in [4, 5], the multilayer design suffered thick profile, complicated structure and high-cost fabrication. As to the bandwidth enhancement of baluns, we have also witnessed several approaches such as using broadband Schiffman phase shifter [3], slot-coupled microstrip lines [6], substrate integrated waveguide [8], phase-adjusting CRLH TL [7] and metamaterial TL [10]. Nevertheless, these baluns occupy a large circuit area. The lack of techniques regarding simultaneous bandwidth and miniaturization make the design of compact broadband balun a pressing task. Here, a compact broadband balun is proposed using fully artificial fractal-shaped CRLH TL [12] and we will begin with the theorem of CRLH TL for broadband objective.

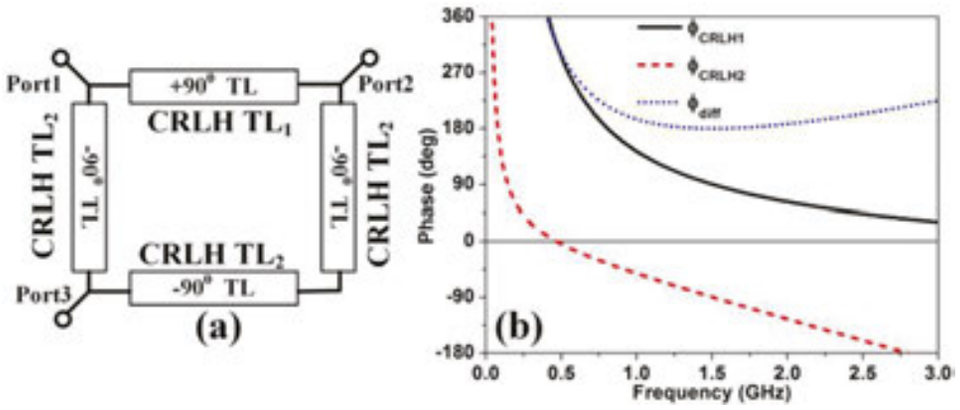

Figure 2. (a) Scheme topology of proposed balun and (b) phase response of dual branches. The derived circuit parameters are: L_{R1} = 0.62 nH, C_{R1} = 0.125 pF, L_{L1} = 8.63 nH, C_{L1} = 1.73 pF, L_{R2} = 6.5 nH, C_{R2} = 1.3 pF, L_{L2} = 89.9 nH, and C_{L2} = 18 pF.

Figure 2 shows the scheme of proposed balun along with the phase response of corresponding dual CRLH branches. Different from branch-line balun with two –90° and two –180° branches, our balun contains one +90° and three –90° TL branches. The characteristic impedance of +90° branch is denoted as Z_{c1} and that of –90° branch as Z_{c2}. To engineer a good impedance match, Z_{c1} and Z_{c2} are related with port impedance Z_0 as [9]

$$Z_{C1} = \frac{Z_{C2}}{\sqrt{2}Z_{C2} - Z_0} Z_0 \tag{3}$$

For simplicity, we select $Z_{C1} = Z_{C2} = \sqrt{2}Z_0$ and Z_0 = 50 Ω. The above four TL branches with specified phase response tailored at a given band can be easily realized through CRLH TL. For convenience, we denote the +90° CRLH branch as CRLH TL_1 while the –90° one as CRLH TL_2. The phase shifts $\varphi_{\text{CRLH TL1}}$ and $\varphi_{\text{CRLH TL2}}$ are explicit functions of the angular frequency ω:

http://dx.doi.org/10.5772/65603

$$\varphi_{\mathrm{CRLH.TL}}(\omega) = -N[\omega\sqrt{L_R C_R} - \frac{1}{\omega\sqrt{L_L C_L}}], \tag{4}$$

Here, N is the number of adopted CRLH atoms and is chosen as 2 in this work. For good impedance match, the following conditions are compulsorily satisfied:

$$\sqrt{\frac{L_{R1}}{C_{R1}}} = \sqrt{\frac{L_{L1}}{C_{L1}}} = \sqrt{\frac{L_{R2}}{C_{R2}}} = \sqrt{\frac{L_{L2}}{C_{L2}}} = \sqrt{2}Z_0 \tag{5}$$

To maximize the bandwidth around f_0 = 1.5 GHz, identical slope of phase response between CRLH TL_1 and CRLH TL_2 must be fulfilled, which indicates that the phase difference φ_{diff} is minimum at angular frequency ω_0:

$$\varphi_{\mathrm{diff}} = -N[\omega\sqrt{L_{R1}C_{R1}} - \frac{1}{\omega\sqrt{L_{L1}C_{L1}}}] + N[\omega\sqrt{L_{R2}C_{R2}} - \frac{1}{\omega\sqrt{L_{L2}C_{L2}}}] \tag{6}$$

To mathematically guarantee above requirement, the first-order derivative of φ_{diff} with respect to ω should be zero whereas the second-order one should be positive, this yields

$$N[\sqrt{L_{R2}C_{R2}} - \sqrt{L_{R1}C_{R1}} + \frac{1}{\omega_0^2\sqrt{L_{L2}C_{L2}}} - \frac{1}{\omega_0^2\sqrt{L_{L1}C_{L1}}}] = 0 \tag{7}$$

$$\frac{2}{\omega_0^3\sqrt{L_{L1}C_{L1}}} - \frac{2}{\omega_0^3\sqrt{L_{L2}C_{L2}}} > 0 \tag{8}$$

The second derivative ensures the extremum of Eq. (5) to be a minimum. We have seven individual equations from Eqs. (4), (5) and (7) but have eight unknowns. Therefore, it is impossible to exclusively determine a group of solution. This additional degree of freedom can be utilized for other purpose in design of the broadband balun with fully artificial TLs.

Here, C_{L2} is first chosen as a marketable chip capacitor with discrete capacitance of 18 pF. Then, residual elements are obtained by solving above equations conducted in mathematical software Matlab. Since many groups of solution (typically 16) would exist due to the square root equations, we rule out all solutions with negative values and followed by a proof-test process to select the physically meaningful one. To conceptually validate the proposal, we adopted the lumped elements derived by this method to calculate the phase response of CRLH TL_1 and CRLH TL_2, see **Figure 2(b)**. As is shown, the slope of both transmission phases is almost the same over a wide frequency region in vicinity of 1.5 GHz. Therefore, the phase difference is almost with a flat response around 180° across a wide band.

For verification, we designed, fabricated and measured a proof-of-concept sample on F4B substrate with thickness of h = 1 mm, dielectric constant of ε_r = 2.65 and loss tangent of tan δ = 0.001. The basic structure we used is trapezoidal Koch curve (T-Koch), see **Figure 3(a)**, which is determined by its iteration factor (IF = 1/4), Hausdorff dimension (ln5/ln4) and iteration order (IO). It should be highlighted that the T-Koch is very beneficial to load SMT capacitors at its horizontal fractal segments. Since the ML of CRLH TL_1 is too short to be constructed in fractal,

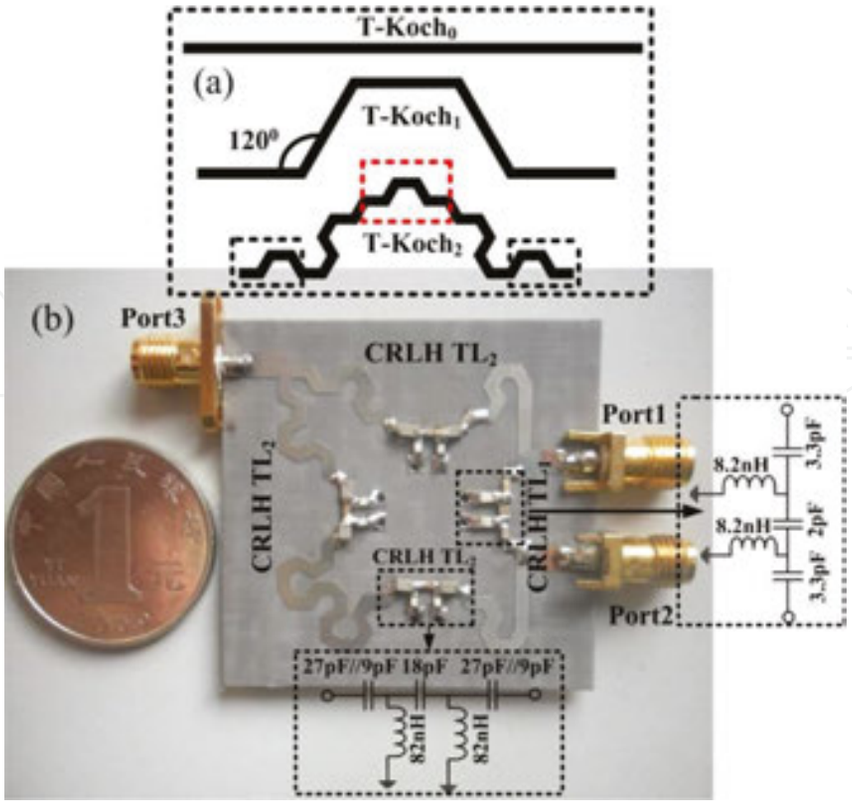

Figure 3. (a) T-Koch curves with zeroth, first and second iteration order and (b) fabricated prototype of the developed balun.

we only considered changing the orientation of several chamfered bends outlined in the black dashed of the T-Koch$_2$ to maximize the miniaturization. The straight length (L_n) and the number of fractal segments (P_n) after n iterations are $L_n = (4/5)^n L_0$ and $P_n = 5^n$, respectively, where L_0 is the initial length. Since T-Koch with higher IO contributes less to the miniaturization while inversely more to fractal segments, the applied T-Koch curve is limited to IO = 2. To load three chip capacitors, five segments outlined in the red dashed of T-Koch$_2$ are removed. Using the established methodology, the ML length of CRLH TL$_1$ and CRLH TL$_2$ is eventually obtained as 3.6 and 40.9 mm, respectively. In the fabricated prototype shown in **Figure 3(b)**, two *T*-type cells with chip capacitors and inductors of 0805 and 0603 packages provided by Murata Manufacturing Company Ltd. are cascaded to build the LH part of two-cell CRLH TL. For easy impedance match and enhanced transmission performance, the CRLH TL is terminated in two capacitors of $2C_L$. The size of the balun is only 29 × 30.5 mm^2, corresponding to 24.5% of π × 33.9 × 33.9 mm^2 that conventional rat-race balun occupies and to 56.4% of the 32 × 49 mm^2 that CRLH balun without fractal perturbation occupies.

The performance of developed balun is characterized through the dynamic links and solver of planar EM and circuit cosimulation in MOM-based Ansoft Designer and is measured by the *Anritsu ME7808A* network analyzer. **Figure 4** shows the simulated and measured *S*-parameters along with amplitude and phase imbalance, which are in good consistency. Slightly larger amplitude imbalance in measurements is mainly attributable to the nonideal SMT chip

http://dx.doi.org/10.5772/65603

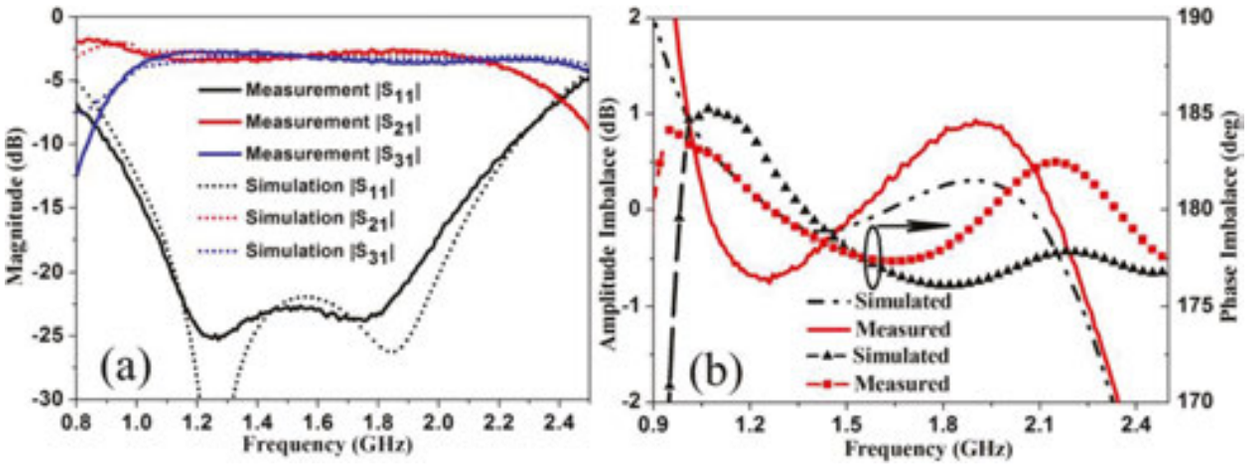

Figure 4. (a) Simulated and measured *S*-parameters of the proposed balun and (b) simulated and measured amplitude and phase imbalance.

components with inductance or capacitance variation of ±10% and is partially to the tolerances inherent in fabrications.

Measurement results reveal that return loss $|S_{11}|$ is better than –10 dB from 1 to 2.25 GHz (a bandwidth of 83.3%), over which the amplitude imbalance varies within 1 dB and the phase differences ranges from 177.3° to 183.4° (180° ± 3.4°). Moreover, the insertion loss $|S_{21}|$ varies between –2.9 and –3.6 dB while $|S_{31}|$ between –2.8 and –3.8 dB. The bandwidth of balun using bare T-Koch fractal is obtained only 10% which is far insufficient relative to proposed design using hybrid technique. To our best knowledge, the proposed balun exhibits comparable performance in broadband and compact size among the available data using double-layer printed circuit board.

To sum up, the insertion loss mainly induced by fractal bends is moderate within the operation band. The hybrid technology of fractal and CRLH TL does not pose severe penalty on device performances but allows additional degree of freedom in developing devices with high integration, promising an elegant alternative for compact and multifunctional devices with high performances.

1.2.2. Dual band rat-race coupler

Rat-race coupler (RRC), see the circuit topology shown in **Figure 5(a)**, is one type of 180° hybrids and one of the most important microwave passive devices. The four-port lossless reciprocal network consists of three –90° branches and one –270° branch with characteristic impedance of $\sqrt{2}Z_0$, where Z_0 is the port impedance 50 Ω. A RRC commonly exhibits two functionalities, namely, a power divider and a power combiner. As a power divider, it can work in two cases of in-phase and 180° out-of-phase state. In the former case, a signal inputted in port 1 divides equally into ports 2 and 3 with identical phase and port 4 is isolated, whereas in the latter case a signal injected into port 4 separates evenly in ports 2 and 3 with 180° phase difference and port 1 is isolated. As a power combiner, two signals with 0°/180° phase difference are input simultaneously at ports 2 and 3 and the sum of signals will be formed at port 1/

port 4. The RRC with four pairs of transmission channel and two pairs of isolation channel (ports 1 and 4, ports 2 and 3) can be modeled by the following scatting matrix [*S*].

$$[S] = \frac{j}{\sqrt{2}} \begin{bmatrix} 0 & 1 & 1 & 0 \\ 1 & 0 & 0 & -1 \\ 1 & 0 & 0 & 1 \\ 0 & -1 & 1 & 0 \end{bmatrix} \tag{9}$$

Multiband components with miniaturized dimensions have aroused a wide of interest since they enable low cost, high reliability and integrity. Up to date, numerous approaches have been developed for compact RRCs, e.g., using capacitor [13] and periodic slow-wave loading [14], using periodic stepped-impedance ring resonators [15], T-shaped photonic bandgap (PBG) structures [16] and fractal strategy [17–19]. Although above RRCs feature compact, the lack of dual band (DB) performances deserves further improvements. To date, much fewer literatures were devoted to DB applications, e.g., using tri-section branch-line [20], stepped-impedance-stub units [21] and two T-shape open-stub units [22]. However, the design and realization were tedious and typically featured large circuit size. The lack of literature concerning both the DB performance and size reduction makes the design of a compact DB RRC a pressing task.

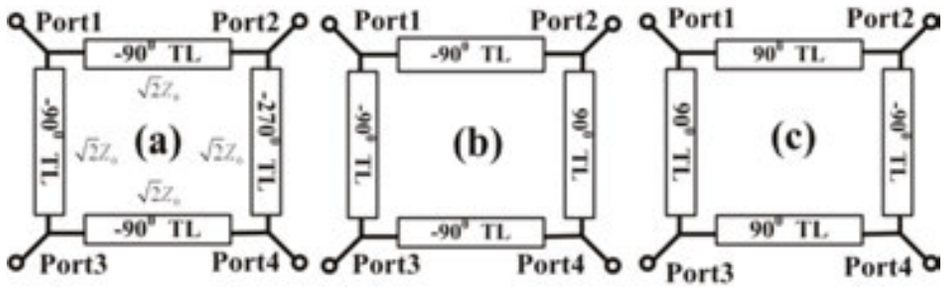

Figure 5. Circuit schematics of the RRCs: (a) conventional one; derivative ones with (b) one +90° branch, and (c) three +90° branches.

In this work, we proposed a novel DB RRC based on the hybrid approach of fractals and CRLH TLs [23]. A new scheme for DB design is proposed by combining two circuit topologies with different phased branches. We noticed that another two RRCs with topologies shown in **Figure 5(b)** and **(c)** also exhibit the same functionality. To develop a DB RRC, we consider combing two of them in one circuit board. Among all three possible combinations, the two networks shown in **Figure 5(a)** and **(c)** are examined as the exclusive solution for DB performance. Two types of CRLH branches with specified phases at two arbitrary frequencies are necessary to integrate these networks. This distinguishes our design from any previous DB synthesis for other devices [24, 25] which only required one set of CRLH branch. Consequently, DB RRC design is less direct and more complicated than any other DB device design, giving rise to the rarely reported work. In this particular design, the operation frequencies are designed at f_L = 0.75 GHz and f_H = 1.8 GHz, respectively.

http://dx.doi.org/10.5772/65603

In what follows, we begin with the dispersion of CRLH TL to briefly derive the fundamental DB theory. At f_L, the RRC works at the state in **Figure 5(c)** with three +90° branches and one –90° branch, whereas at f_H it operates at the state in **Figure 5(a)** with three –90° branches and one –270° branch. For convenience, we denote the CRLH branch with +90° at f_L while –90° at f_H as CRLH TL_1, whereas CRLH TL_2 is the CRLH branch with –90° at f_L while –270° at f_H. Consequently, the DB RRC is formed by three CRLH TL_1 and one CRLH TL_2. Here, φ_L and φ_H are the required phases at f_L and f_H, respectively:

$$\varphi^{\mathrm{CRLH}}(\omega = \omega_L = 2\pi f_L) = \varphi_L \tag{10a}$$

$$\varphi^{\mathrm{CRLH}}(\omega = \omega_H = 2\pi f_H) = \varphi_H \tag{10b}$$

Combining Eqs. (4), (5) and (10), we can readily obtain explicit expressions of four circuit parameters as [25]

$$L_R = \frac{Z_c[\varphi_L(f_L/f_H) - \varphi_H]}{2\pi N f_H[1-(f_L/f_H)^2]}, \tag{11a}$$

$$C_R = \frac{\varphi_L(f_L/f_H) - \varphi_H}{2\pi N f_H Z_c[1-(f_L/f_H)^2]}, \tag{11b}$$

$$L_L = \frac{N Z_c[1-(f_L/f_H)^2]}{2\pi f_L[\varphi_L - \varphi_H(f_L/f_H)]}, \tag{11c}$$

$$C_L = \frac{N[1-(f_L/f_H)^2]}{2\pi f_L Z_c[\varphi_L - \varphi_H(f_L/f_H)]}. \tag{11d}$$

To preserve L_R and C_R positive, the following condition should be satisfied:

$$\varphi_L f_L \geq \varphi_H f_H \tag{12}$$

Following Eq. (12), the possible solution by combining circuit topologies shown in **Figure 5(b)** and **(c)** can ruled out for DB synthesis. Given determined circuit parameters, see **Table 1**, we can readily design the final RRC layout using the approach described in Section 1.1. The

TL type		L_L (nH)	C_L (pF)	$2C_L$ (pF)	L_R (nH)	C_R (pF)	ϕ^{RH} (deg)	P	W
CRLH TL_1	TC	11.1	2.2	4.4	8.42	1.68	–64.3	49.1	1.5
	PU	12	2	4.7					
CRLH TL_2	TC	63.1	12.6	25.2	15.3	3.1	–117.2	89.6	1.5
	PU	56 + 6.8	12	12 + 12					

Note: TC means theoretically computed and PU means practically used, *P* and *W* are length and width of the ML in mm.

Table 1. Detailed circuit parameters and dimensions of ML of the designed CRLH TLs.

designed RRC is built on F4B substrate with ε_r = 2.65, h = 1 mm and tan δ = 0.001 based on standard printed circuit board (PCB) fabrication process.

Figure 6 shows the finally engineered layout of the fractal-shaped RRC. Again, we consider realizing the RH and LH part of the 70.7 Ω CRLH branches by MLs and SMT chip elements, respectively. In the former case, the MLs are configured in Koch shape of *IF* = 1/4 and *IO* = 2 to facilitate a super compact size. The middle fractal sections are removed to load SMT capacitors and the right-angle bends are replaced by chamfered ones to minimize current discontinuity. In the latter case, two cascaded T-networks depicted in **Figure 6(c)** are adopted. Since the necessary space accommodating CRLH TL_1 is much smaller than that of CRLH TL_2, we changed orientations of several chamfered bends of CRLH TL_2 to facilitate a super compact circuit. As appreciated from **Figure 6(a)** and **(b)**, the proposed DB RRC occupies a square area of 52.2 × 39.4 mm^2 and is only 10.2% of 150 × 135 mm^2 that its conventional circular counterpart occupies. Therefore, our hybrid technology shrinks the circuit by 89.8%.

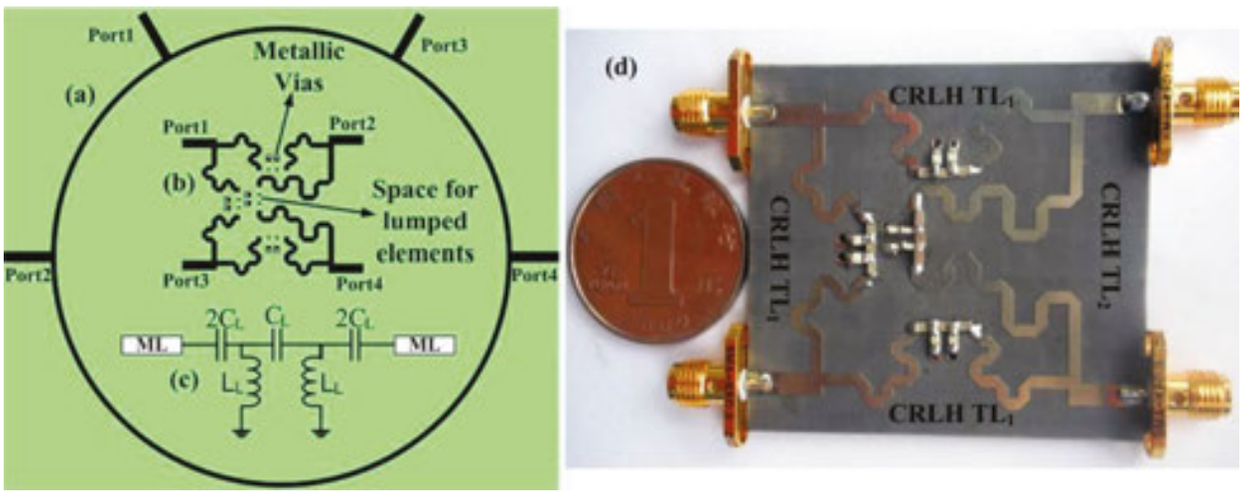

Figure 6. Circuit configuration of the RRCs: (a) conventional design, (b) novel design, (c) circuit topology for LH part of two-cell CRLH TLs, and (d) fabricated prototype.

For characterization, the eventually designed DB RRC is analyzed through the dynamic links and solver of planar EM and circuit cosimulation in Ansoft Designer. For verification, the fabricated RRC sample, see **Figure 6(d)** is measured by *Anritsu ME7808A* vector network analyzer. The SMT chip capacitors and inductors with 0805 and 0603 packages are adopted in prototype fabrication. **Figures 7** and **8** portray the *S*-parameters for in-phase and out-of-phase operation, respectively. In both cases, a reasonable agreement of results between simulation and measurement is observed across the entire frequency band of interest, confirming the effectiveness of our design. The DB performance occurs clearly around 0.75 and 1.8 GHz. For in-phase operation at 0.75 GHz, the measured $|S_{11}|$ is 24.2 dB, $|S_{21}|$ and $|S_{31}|$ are 3.4 and 3.1 dB and $|S_{41}|$ is 28.3 dB, whereas at 1.8 GHz, the measured $|S_{11}|$ is 19.9 dB, $|S_{21}|$ and $|S_{31}|$ are 3.2 and 3.5 dB and $|S_{41}|$ is 28.5 dB. The out-of-phase performance at 0.75 and 1.8 GHz is similar to the in-phase case and is not discussed for brevity of contents. The slight frequency

http://dx.doi.org/10.5772/65603

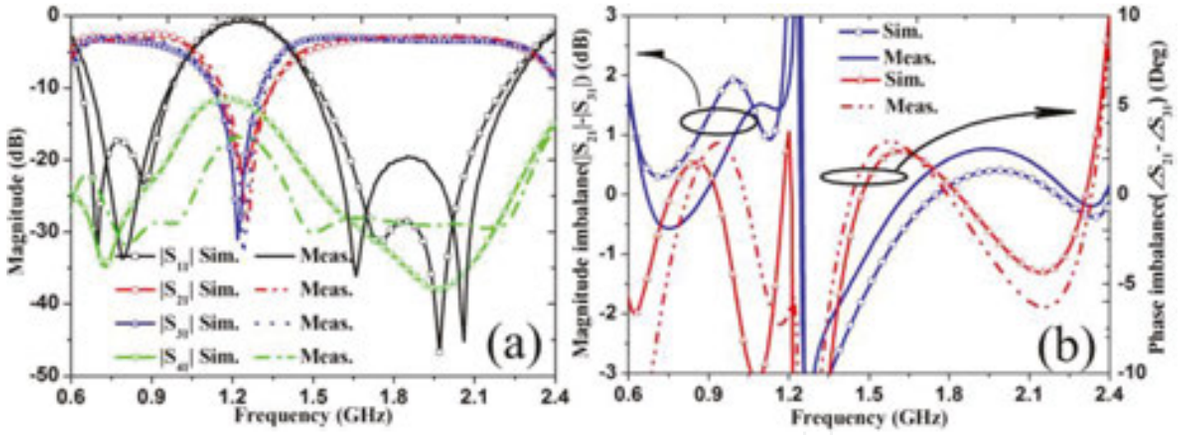

Figure 7. Comparison of *S* parameters between simulation and measurement for in-phase operation: (a) magnitude and (b) output magnitude imbalance and phase imbalance.

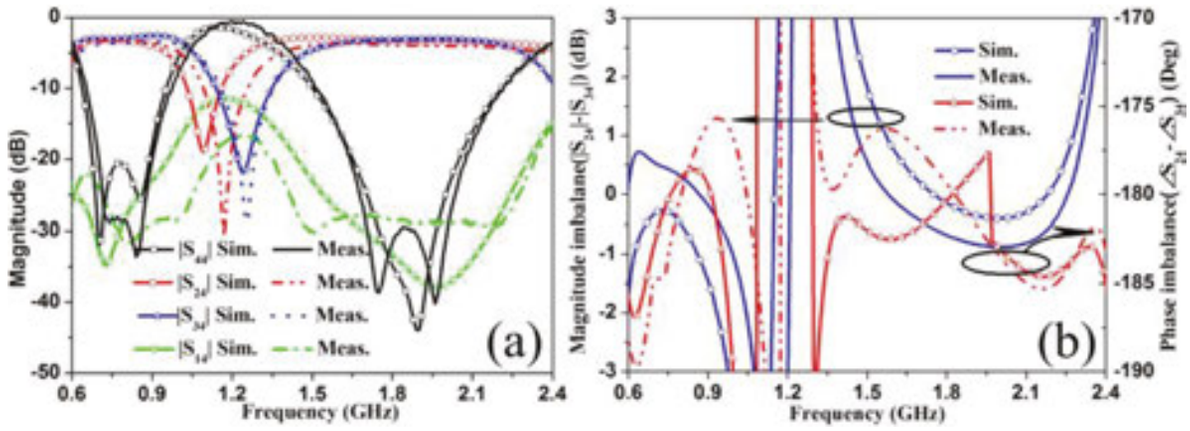

Figure 8. Comparison of *S* parameters between simulation and measurement for 180° out-of-phase operation: (a) magnitude and (b) output magnitude imbalance and phase imbalance.

shift of the first band toward higher frequencies in the measurement case is the same as that discussed in Section 1.2.1. Nevertheless, the discrepancy is within an acceptable range.

Tables 2 and **3** detail the simulated and measured results for both in-phase and out-of-phase operation. In the former case, measured results indicate that $|S_{11}| > 15$ dB, $|S_{21}|$ and $|S_{31}| < 5$ dB, $|S_{41}| > 20$ dB and magnitude and phase imbalances varying within 1 dB and 5° are obtained from 0.73 to 0.92 GHz. Therefore, a fractional bandwidth (FBW) of 190 MHz (a relative bandwidth of 25.3%) is achieved around f_L, whereas a FBW of 26.7% is obtained from 1.56 to 2.04 GHz around f_H. In the latter case, a FBW of 32% characterized by $|S_{44}| > 15$ dB, $|S_{24}|$ and $|S_{34}| < 5$ dB, $|S_{14}| > 20$ dB and magnitude and phase imbalances varying within 1 dB and 5° is acquired from 0.69 to 0.93 GHz around f_L while a FBW of 28.3% from 1.59 to 2.1 GHz is achieved around f_H. In general, the developed DB RRC demonstrated with a modest operation bandwidth and excellent in-band performances in terms of low insertion loss and return loss should be highlighted.

		RL	IL	Isolation	MI	PI
CF_1	Sim.	18.2	2.9 and 3.3	33.1	0.35	–0.3
	Meas.	24.2	3.4 and 3.1	28.3	–0.4	–4.2
FBW_1	Sim.	0.66–0.94	0.61–0.99	0.57–0.97	0.62–0.87	0.66–0.99
	Meas.	0.7–0.92	0.64–1.01	0.54–1.1	0.63–1	0.73–1.1
CF_2	Sim.	29.3	3.1 and 3.2	33.3	0.15	0.5
	Meas.	19.9	3.2 and 3.5	28.5	0.6	–0.15
FBW_2	Sim.	1.58–2.14	1.48–2.29	1.45–2.31	1.57–2.44	1.4–2.36
	Meas.	1.56–2.16	1.46–2.3	1.11–2.33	1.5–2.4	1.37–2.04

Table 2. Detailed in-phase performances of the proposed RRC.

		RL	IL	Isolation	MI	PI
CF_1	Sim.	21.6	3.27 and 2.97	33.1	–0.29	–0.29
	Meas.	28.4	3.25 and 3.7	28.4	0.43	–3.3
FBW_1	Sim.	0.66–0.91	0.62–0.96	0.56–0.96	0.62–0.86	0.66–0.96
	M	0.68–0.93	0.63–1	0.54–1.12	0.58–0.99	0.69–1.09
CF_2	Sim.	34.8	3.2 and 3.1	33.3	–0.15	–0.34
	M	31.7	3.89 and 3.22	28.57	–0.67	0.6
FBW_2	Sim.	1.58–2.11	1.49–2.29	1.46–2.31	1.57–2.28	1.34–2.39
	M	1.59–2.13	1.46–2.28	1.36–2.33	1.47–2.31	1.31–2.1

Note: RL/IL is return/insertion loss in dB, while MI and PI are magnitude imbalance in dB and phase imbalance in degree. FBW_1 and FBW_2 are bandwidth around f_L and f_H in GHz characterized by $|S_{11}|/|S_{44}| \geq 15$ dB, $|S_{21}|$ and $|S_{31}| \leq 5$ dB or $|S_{24}|$ and $|S_{34}| \leq 5$ dB, $|S_{41}| \geq 20$ dB, $|MI| \leq 1$ dB, and $|PI| \leq 5°$.

Table 3. Detailed out-of-phase performances of the proposed RRC.

To sum up, a super compact CRLH RRC is successfully engineered with good DB performances based on proposed DB strategy and hybrid approach. The RRC features low insertion loss, modest operation bandwidth and good isolation between output ports. The 89.8% size reduction is believed to be one of the best miniaturizations in the open literature which should be highlighted.

1.3. Analysis and characterization of novel distributed CRLH atoms

Although lumped-element CRLH TL exhibits the merit of easy design and high degree of freedom, it is rigorously restricted to low-frequency operation due to self-resonant effects of chip components at high frequency. In this subsection, we will introduce a set of distributed resonant-type CRLH TLs made of novel complementary split ring resonators (CSRRs). Three types of CSRRs are involved in terms of compactness, namely complementary single split ring

http://dx.doi.org/10.5772/65603

resonator (CSSRR) pair (CSSRRP), Koch-shaped CSSRRP (K-CSSRRP) and Koch-extended CSSRRP (K-ECSSRRP) [26, 27]. They are investigated in depth based on TL theory and electromagnetic (EM) response characterization, aiming to illustrate the novel working mechanism for miniaturization. Of particular irreverence is the dual-shunt branch circuit theory established for a new set of CRLH TLs.

1.3.1. CSSRRP-loaded CRLH atom

The topology of the first CSRRs-evolved CRLH element is shown in **Figure 9(a)**. As is shown, the CSSRRP etched on the ground is composed of two CSSRRs with face-to-face splits beneath a capacitive gap. When the element operates in LH band where the backward propagation is supported, the CSSRRP responds to the time varying axial electric field and affords a negative permittivity. In the circuit model (losses have been excluded) shown in **Figure 9(c)**, the CSSRRP is described by means of a parallel resonant tank formed by L_p, C_p and C_k. C is contributed by the electrical coupling between the series gap and the CSSRRP and the line capacitance. The residual circuit elements share the same physical meaning with those of conventional CSRRs [28]. Here, we introduce additional capacitance C_k to model the interaction between two CSSRRs. Therefore, our proposal allows additional degree of freedom for design and the circuit model can be treated as a special case of a CSSRR-loaded CRLH atom shown in **Figure 9(b)** when C_k is null. The correctness of our model will be validated by full-wave S-parameters calculated through the commercial MOM (moment of method)-based package Ansoft Designer. For characterization, the F4B substrate with a thickness of h = 0.8 mm and a dielectric constant of ε_r = 2.65 is considered for all simulations and power divider design.

Figure 10 depicts the frequency response of a CSSRRP- and CSSRR-loaded CRLH TLs obtained from EM full-wave simulation and electrical simulation (circuit model) in Ansoft

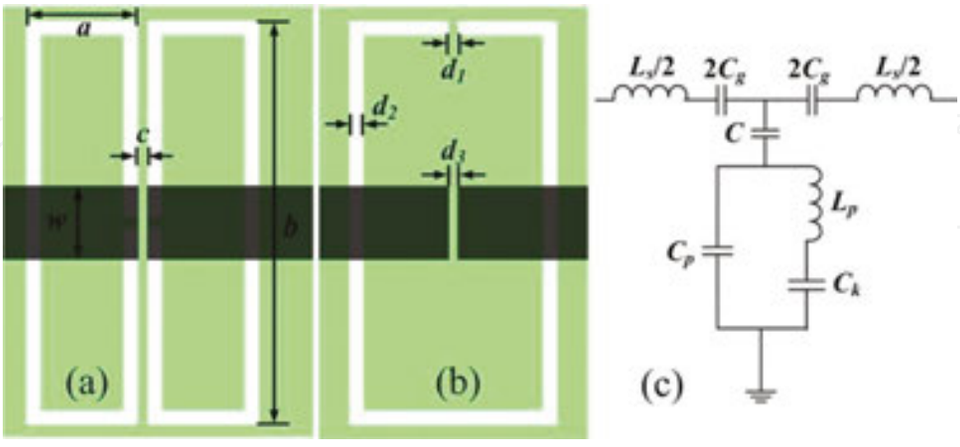

Figure 9. Topology of the: (a) CSSRRP and (b) CSSRR loaded CRLH TLs along with (c) the *T*-type equivalent circuit model. The capacitive gap is etched on the conductor strip (depicted in dark grey), beneath which the CSSRRP and CSSRR (depicted in white) are etched on the ground (depicted in green). Here, the CSSRRP and CSSRR occupy the same size and have d_1 = 0.3 mm, d_3 = 0.2 mm, d_2 = 0.3 mm, b = 9.6 mm, and w = 1.8 mm. For CSSRRP, the metallic spacing between two CSSRR is c = 0.3 mm and a = 2.4 mm.

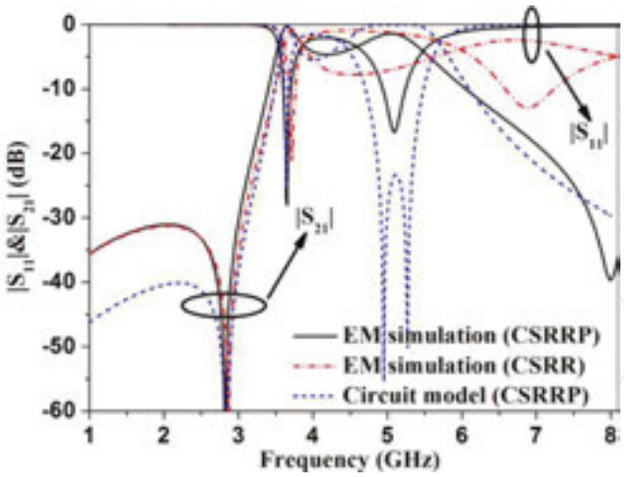

Figure 10. Frequency response of the CSSRRP-loaded and CSSRR-loaded CRLH TL obtained from full-wave EM simulation and electrical simulation. The lumped elements are extracted as L_s = 17.1 nH, L_p = 2.97 nH, C_g = 0.067 pF, C = 363.6 pF, C_p = 1.03 pF, and C_k = 1.06 pF.

Serenade. As is shown, the *S*-parameters of proposed CRLH atom in both cases are in excellent agreement, illustrating the rationality of the model. Moreover, our meta-atom exhibits slightly lower resonance (LH band) and lower transmission zero below relative to CSSRR-loaded one, enabling a more compact subwavelength particle. Moreover, our atom exhibits lower in-band insertion loss for both the LH and RH band (centered at 5.09 GHz). Most importantly, the frequency interval between the LH band and RH band is much narrower than that of the CSSRR-loaded CRLH atom whose RH band is observed at 6.88 GHz. Therefore, it is easier to realize the balanced condition using proposed meta-atom. The sharp transmission zero above the RH band is more suitable for in-band selectivity and out-of-band harmonics suppression. The identification of aforementioned LH and RH bands will be examined through effective constitutive parameters.

The exotic EM behavior of the proposed CRLH atom can be analyzed based on equivalent circuit model inspired by Bloch theory. The series and shunt impedances are given by

$$Z_s(j\omega) = \frac{1-\omega^2 L_s C_g}{j2\omega C_g}, \tag{13}$$

$$Z_p(j\omega) = \frac{(1-\omega^2 L_p C_k)}{j\omega(C_p + C_k) - j\omega^3 L_p C_p C_k} + \frac{1}{j\omega C}. \tag{14}$$

The shunt admittance can be obtained immediately from Eq. (14):

$$Y_p(j\omega) = 1/Z_p(j\omega) = \frac{j\omega C[C_p + C_k - \omega^2 L_p C_p C_k]}{C_p + C_k + C - \omega^2 L_p C_k (C_p + C)} \tag{15}$$

As crucial parameters for circuit design, the electrical length φ and characteristic impedance Z_β of a CRLH TL are determined by

$$\cos\varphi = \cos(\beta l) = 1 + \frac{Z_s(j\omega)}{Z_p(j\omega)}, \tag{16}$$

$$Z_\beta = \sqrt{Z_s(j\omega)[Z_s(j\omega) + 2Z_p(j\omega)]} \tag{17}$$

Thus, by insertion of Eqs. (13) and (14) into Eqs. (16) and (17), the propagation constant β and Z_β are obtained. The EM wave propagation is allowed in the region where both β and Z_β are real and positive values. In what follows, we will discuss the limits of the LH and RH band and finally derive the balanced condition for broadband operation. Similar to CSRRs-loaded CRLH atom [28], the lower limit of the RH band f_{RH}^L corresponds to the resonances of series branch:

$$f_{RH}^L = f_{se} = 1/2\pi\sqrt{L_s C_g} \tag{18}$$

In a similar manner, the transmission zero f_T occurs below the lower limit of LH band f_{LH}^L when the shunt branch resonates, namely Eq. (14) is null or Eq. (15) takes an extreme value:

$$f_T = f_{sh} = \frac{1}{2\pi}\sqrt{\frac{C_p + C_k + C}{(L_p C_k (C_p + C)}} \tag{19}$$

When the parallel tank of CSSRRP resonates, we obtain the upper limit of the LH band f_{LH}^H by forcing Eq. (15) to be zero:

$$f_{LH}^H = f_p = \frac{1}{2\pi}\sqrt{\frac{C_p + C_k}{L_p C_k C_p}} \tag{20}$$

Here, Eqs. (18) and (20) are reasonable on assumption that $f_p \leq f_{se}$. If $f_p > f_{se}$, f_{RH}^L and f_{LH}^H interchange their value. Under balanced condition $f_{LH}^H = f_{RH}^L = f_0$, the LH band transits to the RH one continuously without a gap. We can obtain f_{LH}^L and the upper limit of RH band f_{RH}^H when Eq. (17) is null. The analytic expressions for f_{LH}^L and f_{RH}^H are tedious and hence are not reproduced here. However, they are revealed in **Figure 11** through series impedance, shunt admittance and characteristic impedance calculated using the extracted circuit parameters shown in the caption of **Figure 10**.

Referring to **Figure 11**, Y_p is null at 4.03 GHz (f_{LH}^H) and takes extreme value at 2.83 GHz (f_T) which coincide well with f_T = 2.82 GHz obtained in **Figure 10**. Moreover, Z_{se} is observed as null at 4.71 GHz (f_{RH}^L) and therefore a stop band emerges in the unbalanced case as $f_{LH}^H \neq f_{RH}^L$. In addition, Z_β takes zero value at 3.61 (f_{LH}^L) and 5.59 GHz (f_{RH}^H). Within 3.61~4.03 GHz, Z_β/β takes positive/negative real number which reveals a LH transmission, whereas within 4.03–4.71 GHz both Z_β and β take pure imaginary value which represents loss and a stop band. Finally, both Z_β and β are positive real numbers within 4.71–5.59 GHz, indicating a RH transmission. In general, the results in **Figure 11** coincide well with those in **Figure 10**.

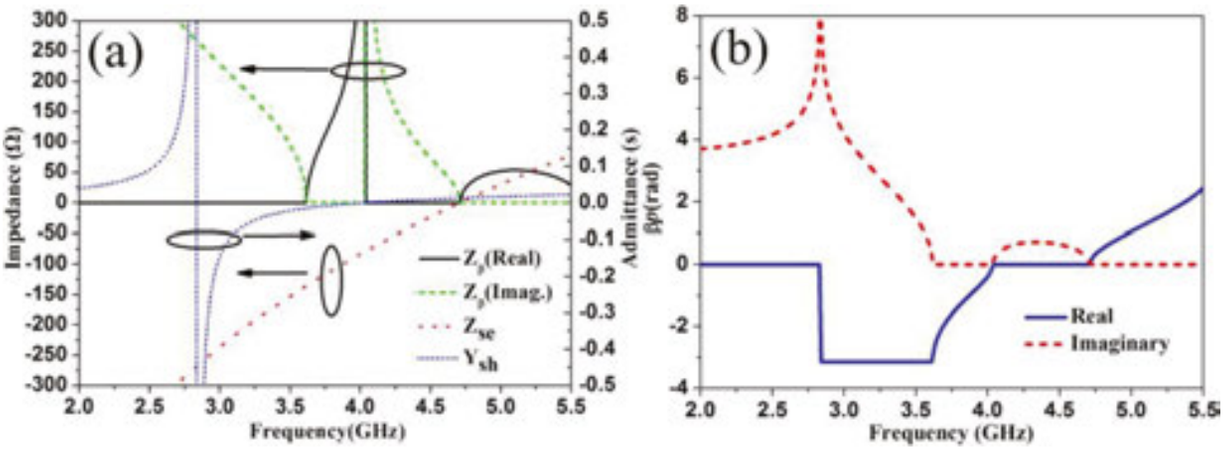

Figure 11. Representation of: (a) series impedance, shunt admittance, and characteristic impedance versus frequency and (b) propagation constant of the CSSRRP-loaded unbalanced CRLH TL in Figure 9.

Figure 12 illustrates the extracted effective constitutive parameters of the CSSRRP-loaded CRLH atom. Negative refractive index and propagation constant can be clearly observed within 2.74–3.94 GHz. The LH band that allows signals to be transmitted freely is observed within 3.56–3.94 GHz, where the imaginary parts of refractive index, permittivity and permeability approximate to zero. However, the imaginary parts associated with electric or magnetic loss are considerable within 2.74–3.56 GHz where the EM wave propagation is still not allowed. A further inspection reveals that an obvious electric resonance occurs around 3.6 GHz with negative permittivity. The vanished electric resonance for the meta-atom without CSSRRP illustrates that the new slot gives rise to the negative permittivity. Since the effective permeability is negative across the entire band, the simultaneous negative LH band is solely dependent on the negative permittivity band (3.56– 3.94 GHz). The retrieved β is consistent with φ obtained from Bloch analysis except for the magnitude discrepancy which is inherently introduced by the multiplication factor l in Eq. (4). In general, the constitutive EM parameters interpreted all exhibited EM phenomena.

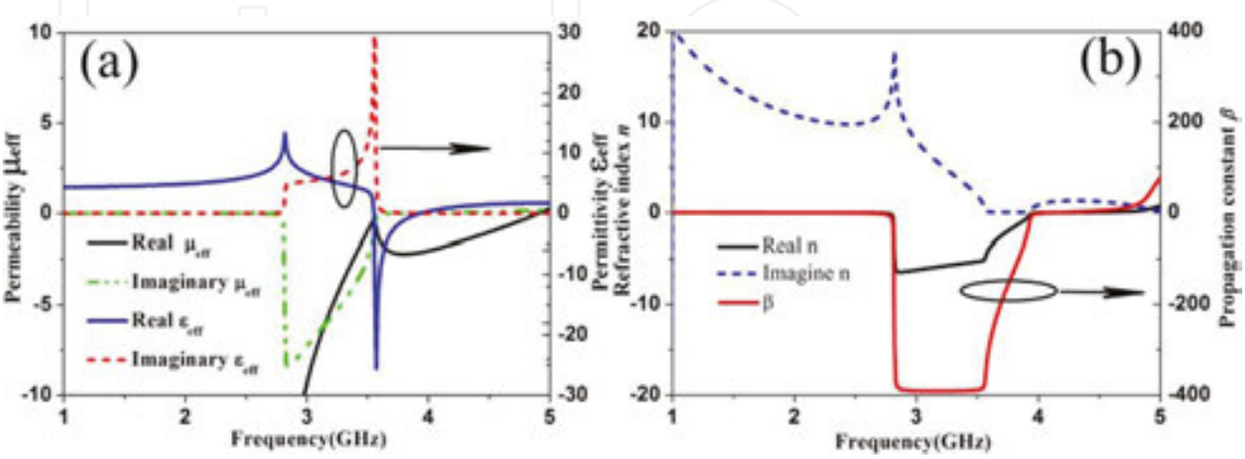

Figure 12. The effective constitutive EM parameters of the CSSRRP-loaded CRLH TL: (a) effective permittivity and permeability and (b) refractive index n and propagation constant β.

http://dx.doi.org/10.5772/65603

Our further numerical results (not included here for brevity) show that LH band shifts downwards when either width a or length b increases. The increase of a and b enhances both C_P and C. However, the in-band insertion loss increases drastically and the LH band may even vanish. The influence of the series gap and microstrip line is analogous to that of conventional CSRRs [28] and thus is not discussed. Most importantly, it is easier to engineer a balanced condition when $2a \approx b$ is guaranteed. In this case, the CRLH meta-atom may exhibit an inherent balanced point. Nevertheless, such balanced point is nonexclusive which will be validated below.

1.3.2. KCSSRRP-loaded CRLH atom with balanced condition

Since the LH band of above CRLH atom is narrow, it is preferred for narrow-band filter applications. Moreover, the potential for further miniaturization of CSSRRP-loaded CRLH atom is still available. Here, we will improve the in-band bandwidth and demonstrate the zero-phase behavior by engineering a miniaturized balanced CRLH TL.

As discussed earlier, the position of RH band is much influenced by a and b. As such, we construct the slot of CSSRRP in Koch curve for other demand and further miniaturization. The new K-CSSRRP shares the same operation mechanism with CSSRRP and thus exhibits similar LH characteristic. The Koch slot of zig-zag boundary significantly extends the current path in ground plane, namely, increases the electrical wavelength in terms of an enhanced C_p. To facilitate a balanced condition ($f_{LH}^{H} = f_{RH}^{L} = f_0$), a low-impedance patch is introduced in the upper conductor line to increase L_s and C_g and thus shifts the RH band downwards. Moreover, it is advisable to maintain the C as a small value to preserve the LH characteristic with low loss.

In the first design example (see **Figure 13**), the K-CSSRRP is with partial fractal boundary only by constructing the two outmost vertical sides as Koch curves of third order. **Figure 14** depicts

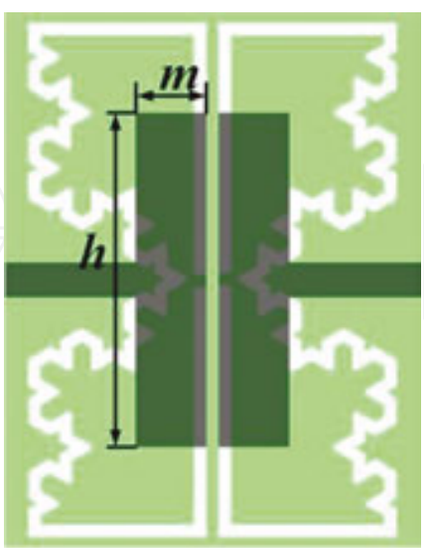

Figure 13. Layout of K-CSSRRP-loaded zero phase-shift CRLH TL operating at Satellite DMB band. The characteristic impedance corresponds to 50 Ω and detailed geometrical parameters are a = 4 mm, b = 12 mm, c = 0.3 mm, $d_1 = d_2 = d_3$ = 0.3 mm, m = 1.7 mm and h = 8 mm. The width of microstrip line is 0.83 mm. The IF of Koch curve is 1/3.

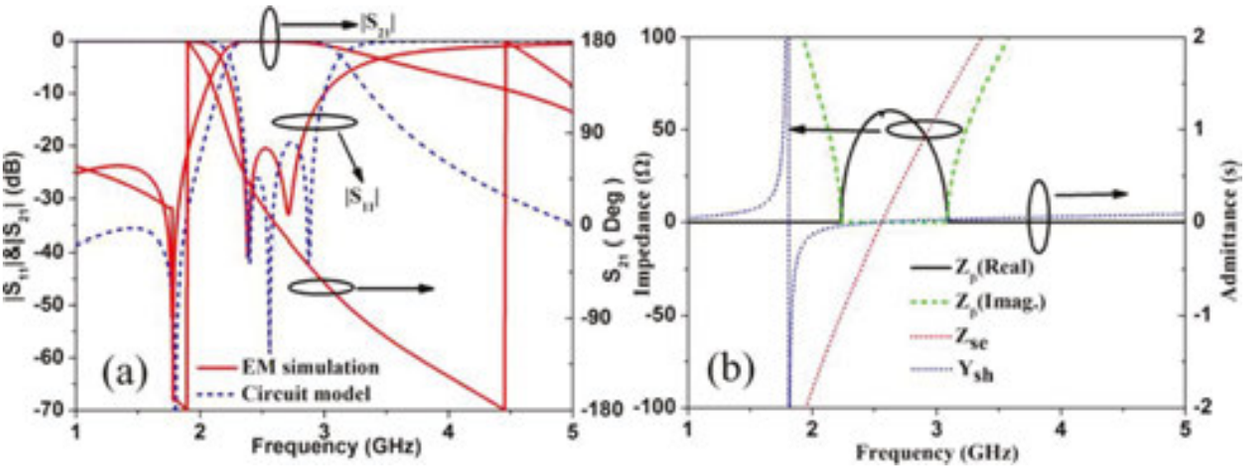

Figure 14. (a) *S*-parameters and (b) representation of series impedance, shunt admittance, and characteristic impedance of the K-CSSRRP-loaded balanced zero phase-shift CRLH atom. The extracted lumped elements are: L_s = 22.5 nH, L_p = 2.36 nH, C_g = 0.172 pF, C = 369.4 pF, C_p = 3.217 pF, and C_k = 3.34 pF.

the simulated *S*-parameters and the representation of series impedance, shunt admittance and characteristic impedance. From **Figure 14(a)**, a reasonable agreement of results is clearly observed between circuit and full-wave EM simulations. The exact zero phase response is obtained within the Satellite DMB band centered at 2.63 GHz. The balanced condition can be further validated through theoretical analysis results shown in **Figure 14(b)**, where the shunt admittance and series impedance intersect at 2.56 GHz. At this frequency, the LH band transforms to the RH band continuously without a band gap.

In the second design example (see **Figure 15**), the four-vertical and four-horizontal slots are constructed as Koch curves of quasi-second iteration order to roughly guarantee $2a \approx b$ in a square configuration with full fractal boundary. In this regard, a balanced CRLH TL with bandwidth enhancement will be achieved as discussed above. To accommodate all fractal

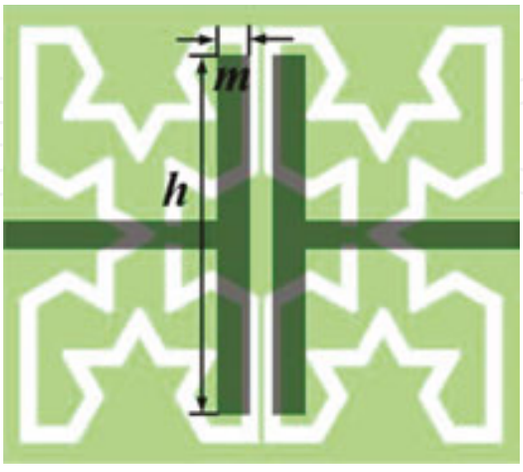

Figure 15. K-CSSRRP-loaded phase-shift CRLH atom with characteristic impedance of 70.7 Ω operated at WiMAX band. The geometrical parameters (in mm) are: a = 4, b = 7.2, c = 0.1, $d_1 = d_2$ = 0.3, d_3 = 0.4, m = 0.6, h = 6.5. The width of microstrip line is 0.5 mm and the iteration factor of Koch slot is 1/3.

http://dx.doi.org/10.5772/65603

sections in a highly compact region for further size reduction, some Koch sections formed in the first-order iteration process are removed. The lumped-element circuit parameters are also extracted for theoretical analysis, see caption of **Figure 16**.

Figure 16 portrays the corresponding frequency response, along with representation of series impedance, shunt admittance and characteristic impedance. From **Figure 16(a)**, it is obvious that *S*-parameters obtained from circuit and EM simulations are in excellent agreement over the entire frequency range, further confirming the correctness of proposed model. The return loss is better than –10 dB from 3.17 to 4.13 GHz and all EM phenomena reveal a balanced pass band without stop band interruption. Moreover, the zero phase shift occurs within WiMAX band centered at 3.5 GHz. From **Figure 16(b)**, Z_β takes a positive real number within the pass band of 3.11–4.22 GHz and the balanced point occurs at 3.52 GHz where the series impedance and shunt admittance intersect on the frequency axis. The transmission zero is always observed below the LH band no matter in balanced or unbalanced case. The fractal perturbation in CSSRRP results in a significant lower operation band whose center frequency reduces from 5.01 (without fractal geometry) to 3.5 GHz. Thus, a frequency reduction of 30.2% is obtained.

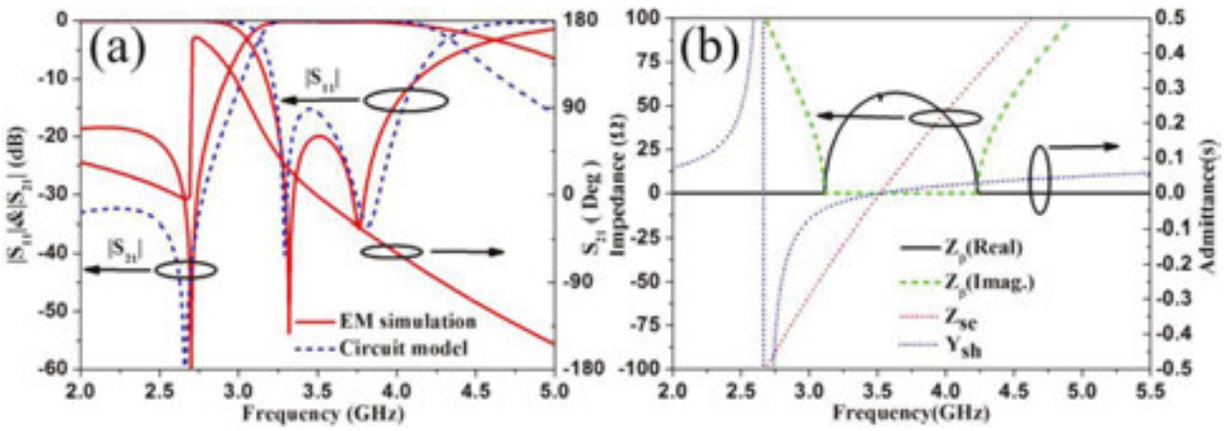

Figure 16. (a) *S*-parameters and (b) representation of the series impedance, shunt admittance, and characteristic impedance of the K-CSSRRP-loaded balanced zero phase-shift CRLH atom. The extracted lumped elements are: L_s = 16.37 nH, L_p = 2.14 nH, C_g = 0.125 pF, C = 159.4 pF, C_p = 2.22 pF, and C_k = 1.68 pF.

1.3.3. K-ECSSRRP-loaded CRLH atom with dual-shunt branch circuit

The objective of this subsection is to establish the theory and design of a new class of CRLH atoms that own dual-shunt branch circuit and enable compact RF/microwave devices with harmonic suppression. As a result, it is unnecessary to cascade a chain of CSRRs for harmonic suppression, which in turn leads to super compact devices.

Figure 17 shows novel dual-shunt brunch circuit model and the layout of novel CRLH atom evolved from previous CSSRRP-loaded CRLH structure. Here, previous CRLH atom, see **Figure 17(a)** is reproduced for comparison convenience. The major difference of novel CRLH atom lies in the K-ECSSRRP etched in the ground, see **Figure 17(b)**. It is constructed by

expanding each end-point of CSSRRP with an inner smaller slot made of three second-order Koch curves and one first-order Koch curve.

Similar to CSSRRP [26], the K-ECSSRRP beneath the capacitive gap excites current along the zig-zag boundary and generates two effects in response to the time varying axial electric field, i.e., the electric excitation to external CSSRRP and that to inner Koch slot. The electric excitation to inner slot is independent of external CSSRRP and thus also provides a shunt branch in the circuit model like CSSRRP. To guarantee effective excitation, the center area of the complementary resonator should be unoccupied. Both excitations contribute to the negative permittivity. In the CM shown in **Figure 17(c)** and **(d)**, losses are irrespective of for analysis convenience. L_s represents the line inductance, C_g models the gap capacitance, CSSRRP is described by means of a parallel resonant tank formed by L_{p1}, C_{p1} and C_{k1}, C_1 contains the line capacitance and the electrical coupling through the gap to CSSRRP. In like manner, the shunt brunch formed by C_2, L_{p2}, C_{p2} and C_{k2} models the corresponding effect of the Koch slot. Consequently, novel CRLH atom enhances considerably the design flexibility.

To begin with, we perform numerical circuit analysis to identify the transmission zeros, cutoff frequencies, LH characteristic and balanced condition. Assume a two-port CRLH TL with N cells, the transmission behavior can be readily predicted using the [*ABCD*] matrix method. Here, the *ABCD* parameters can be easily obtained from *S*-parameters. Provided a [*ABCD*] matrix for a single-cell CTLH atom with known input and output voltage and current, the transmission characteristic of N-cell CRLH TL can be straightly achieved by cascading N two-port networks:

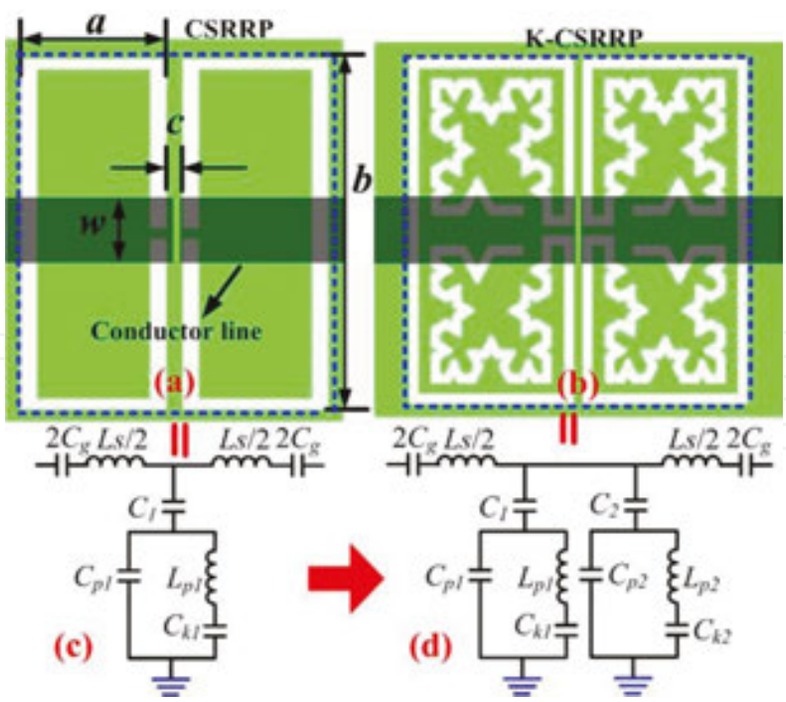

Figure 17. Topology of: (a) the CSSRRP- and (b) K-ECSSRRP-loaded CRLH atoms along with their (c) single-shunt and (d) dual-shunt branch circuit models. Here, the capacitive gap is etched on the conductor line (depicted in lights grey) beneath which, the CSSRRP and K-ECSSRRP (depicted in white) are etched on the ground (depicted in green). Both CRLH atoms have identical slot width 0.3 mm and gap width of 0.2 mm, the residual geometrical parameters are a = 5.3 mm, b = 10.3 mm, c = 0.3 mm, and w = 2 mm.

$$\begin{bmatrix} V_{\text{out}} \\ I_{\text{out}} \end{bmatrix} = \begin{bmatrix} A_N & B_N \\ C_N & D_N \end{bmatrix} \begin{bmatrix} V_{\text{in}} \\ I_{\text{in}} \end{bmatrix} = \prod_{k=1}^{N} \begin{bmatrix} A & B \\ C & D \end{bmatrix}^N \begin{bmatrix} V_{\text{in}} \\ I_{\text{in}} \end{bmatrix} \tag{21}$$

Although CRLH atoms are isotropic and periodic in this design for computational and fabrication convenience, it is unnecessary to require this condition in practice. The [*ABCD*] matrix of a CRLH atom is related with the series impedance Z and shunt admittance Y (Y_1 and Y_2 for each branch) as

$$\begin{bmatrix} A & B \\ C & D \end{bmatrix} = \begin{bmatrix} 1 & Z/2 \\ 0 & 1 \end{bmatrix} \begin{bmatrix} 1 & 0 \\ Y_1 + Y_2 & 1 \end{bmatrix} \begin{bmatrix} 1 & Z/2 \\ 0 & 1 \end{bmatrix} = \begin{bmatrix} 1 + Z(Y_1 + Y_2)/2 & Z[1 + Z(Y_1 + Y_2)/4] \\ Y_1 + Y_2 & 1 + Z(Y_1 + Y_2)/2 \end{bmatrix} \tag{22}$$

Z is formulated as a function of circuit elements:

$$Z = \frac{2(1 - \omega^2 L_s C_g)}{j\omega C_g} \tag{23}$$

The calculation of Y is somewhat tedious and can be attained as

$$Y = Y_1 + Y_2 = \frac{j\omega C_1[C_{p1} + C_{k1} - \omega^2 L_{p1} C_{p1} C_{k1}]}{C_{p1} + C_{k1} + C_1 - \omega^2 L_{p1} C_{k1}(C_{p1} + C_1)} + \frac{j\omega C_2[C_{p2} + C_{k2} - \omega^2 L_{p2} C_{p2} C_{k2}]}{C_{p2} + C_{k2} + C_2 - \omega^2 L_{p2} C_{k2}(C_{p2} + C_2)} \tag{24}$$

Apply the periodic boundary condition to the two-port network, we have $V_{\text{out}} = e^{-i\beta p} V_{\text{in}}$ and $I_{\text{out}} = e^{-i\beta p} I_{\text{in}}$, where p is the physical length of a CRLH atom and β is the propagation constant. Taking this condition together with Eq. (21) yields

$$\begin{bmatrix} A & B \\ C & D \end{bmatrix} \begin{bmatrix} V_{\text{in}} \\ I_{\text{in}} \end{bmatrix} - e^{-i\beta p} \begin{bmatrix} V_{\text{in}} \\ I_{\text{in}} \end{bmatrix} = \begin{bmatrix} A - e^{-i\beta p} & B \\ C & D - e^{-i\beta p} \end{bmatrix} \begin{bmatrix} V_{\text{in}} \\ I_{\text{in}} \end{bmatrix} = 0 \tag{25}$$

The determinant of Eq. (25) should be zero to guarantee a nontrivial solution, which yields [25]

$$AD - (A + D)e^{-i\beta p} + e^{-2i\beta p} - BC = 0 \tag{26}$$

Insertion of Eq. (22) into Eq. (26), we can obtain the dispersion relation associated with Z, Y_1 and Y_2 as

$$\cos(\beta p) = 1 + Z(Y_1 + Y_2)/2. \tag{27}$$

Take the condition of Brillouin zone ($\beta p = \pi$), we immediately have

$$Z(Y_1 + Y_2) = -4 \tag{28}$$

The lower cutoff of LH band $\omega_{LH}^L = 2\pi f_{LH}^L$ and the upper cutoff of RH band $\omega_{RH}^H = 2\pi f_{RH}^H$ can be obtained by solving Eq. (28). In the same time, we obtain the equation of $Z(Y_1 + Y_2) = 0$

when take $\beta = 0$. In this regard, the upper limit of LH band $\omega_{LH}^{H} = 2\pi f_{LH}^{H}$ and lower limit of RH band $\omega_{RH}^{L} = 2\pi f_{RH}^{L}$ are achieved by solving the following equations:

$$\begin{aligned} &C_1[C_{p1} + C_{k1} - \omega^2 L_{p1} C_{p1} C_{k1}][C_{p2} + C_{k2} + C_2 - \omega^2 L_{p2} C_{k2}(C_{p2} + C_2)] \\ &+ \omega C_2[C_{p2} + C_{k2} - \omega^2 L_{p2} C_{p2} C_{k2}][C_{p1} + C_{k1} + C_1 - \omega^2 L_{p1} C_{k1}(C_{p1} + C_1)] = 0 \end{aligned} \tag{29}$$

$$1 - \omega^2 L_s C_g = 0 \tag{30}$$

Moreover, the Bloch impedance Z_β is derived from Eq. (25) after solving Eq. (26) for $e^{-i\beta p}$ and taking reciprocal ($AD - BC = 1$) and symmetric ($A = D$) condition in this particular design:

$$Z_\beta = \frac{V_{\text{in}}}{I_{\text{in}}} = \frac{B}{A - e^{-i\beta p}} = \frac{B}{\sqrt{A^2 - 1}} \tag{31}$$

Insertion of Eq. (22) into Eq. (31) yields

$$Z_\beta = \sqrt{Z[1/(Y_1 + Y_2) + Z/4]} \tag{32}$$

The f_{LH}^{L} and f_{RH}^{H} can be achieved by forcing Eq. (32) to be null. Moreover, two transmission zeros of the two shunt branches are determined when the denominator of Eq. (24) is null:

$$f_{T1} = \frac{1}{2\pi}\sqrt{\frac{C_{p1} + C_{k1} + C_1}{(L_{p1} C_{k1}(C_{p1} + C_1)}}, \tag{33}$$

$$f_{T2} = \frac{1}{2\pi}\sqrt{\frac{C_{p2} + C_{k2} + C_2}{(L_{p2} C_{k2}(C_{p2} + C_2)}}. \tag{34}$$

The CRLH TL is rigorously balanced only when $f_{LH}^{H} = f_{RH}^{L}$ which is particular interest for broadband design. In this case, the LH band (backward wave propagation) switches to the RH region (forward wave propagation) without a gap. Otherwise the continuous pass band is perturbed by a stop band. Rather than obtain cut-off frequencies from tedious analytical expressions by solving Eqs. (28), (29) and (32), we will illustrate them by means of representations of these equations, see **Figure 18**. Moreover, these cutoffs can also be ambiguously identified from transmission zeros of CRLH TLs with large number of cells, see **Figure 19**. Note that f_{LH}^{L} and f_{RH}^{H} do not correspond to the attenuation poles that the two shunt branches afford. In a general case, they fulfill the requirement of $f_{T1} \le f_{LH}^{L} < f_{LH}^{H} \le f_{RH}^{L} < f_{RH}^{H} \le f_{T2}$.

For characterization, **Figure 18(a)** illustrates the *S*-parameters of proposed CRLH atoms obtained from full-wave EM simulation and circuit simulation. The low-loss RT/duroid 4300C substrate with h = 0.5 mm and ε_r = 3.38 is utilized as the dielectric board. As is shown, the results obtained from EM simulation and circuit simulation are in desirable agreements. Therefore, the rationality of the circuit model and lumped parameters are ambiguously verified. Slight discrepancy beyond the upper transmission zero is attributable to the higher-order mode (third attenuation pole) which is not considered in the CM. Novel CRLH atom obviously

http://dx.doi.org/10.5772/65603

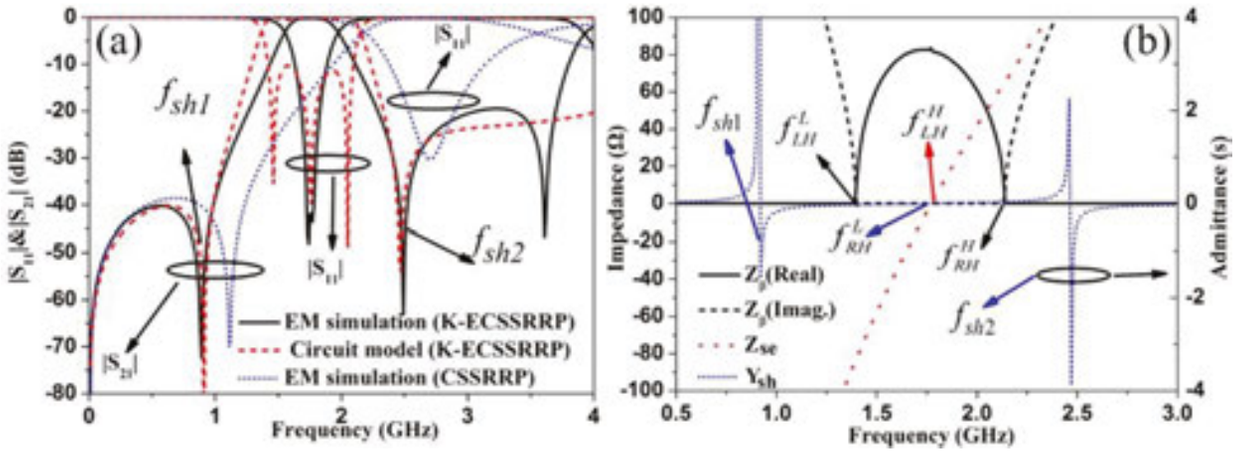

Figure 18. (a) *S* parameters of proposed CRLH atoms and (b) representation of the series impedance, shunt admittance, and characteristic impedance. The extracted circuit parameters are: L_s = 31.02 nH, C_g = 0.26 pF, C_1 = 6.74 pF, C_{k1} = 351.4 pF, C_{p1} = 0.59 pF, L_{p1} = 4.26 nH, C_2 = 1.33 pF, C_{k2} = 2.16 pF, C_{p2} = 0.1 pF, and L_{p2} = 4.84 nH.

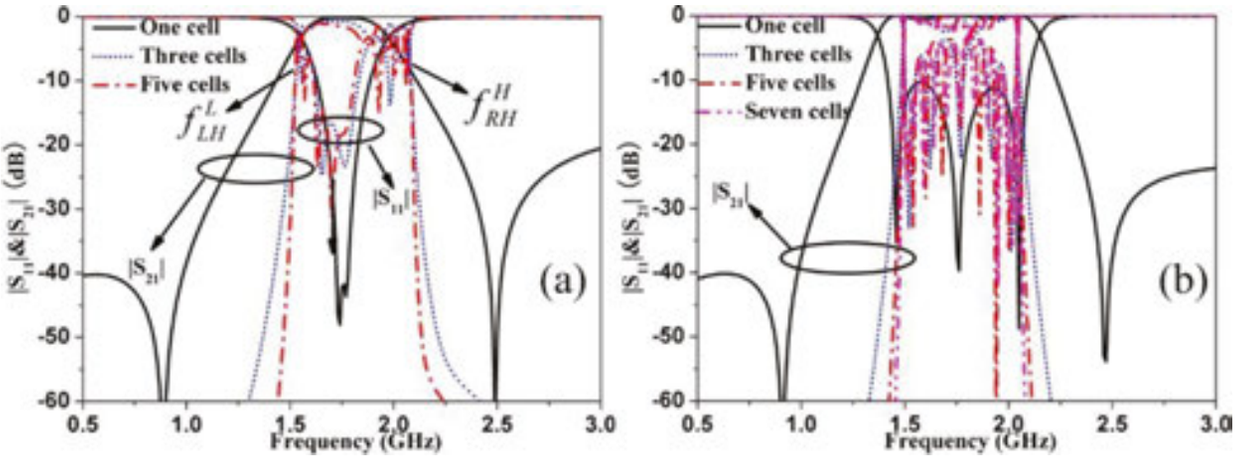

Figure 19. *S*-parameters of proposed CRLH TLs owning different elements: (a) EM full-wave simulation and (b) CM simulation.

exhibits two transmission zeros around 0.9 and 2.48 GHz in the lower and upper edge of pass band, whereas the upper transmission zero is not evidenced for CSSRRP. In addition, the Koch slot also induces a significant red shift of 33%. From **Figure 18(b)**, two transmission zeros related to resonances of Y_1 and Y_2 are expected in both pass band edges where Z_β takes real numbers. It also reveals that the particle works in balanced condition and the resultant transition occurs at the intersection (1.78 GHz) of Y and Z on the frequency axis.

Figure 19 depicts the *S*-parameters of proposed CRLH TLs owning different number of cells. The interval between adjacent cells is chosen as 4.6 mm which is a good tradeoff for homogeneity and inter-element coupling. Both EM and CM simulation results indicate that the signal suppression and selectivity at the lower and upper band have been obviously enhanced with increasing number of cells. Very accurate cutoff frequencies can be identified when $N \geq 3$ in EM simulation while $N \geq 7$ in circuit simulation. The $f^{L}_{LH} = 1.52$ and $f^{H}_{RH} = 2.09$ GHz characterized

by –10 dB suppression in former case are quantitative very similar to $f_{LH}^{L} = 1.48$ and $\omega_{RH}^{H} = 2.05$ GHz in latter case. The ripples in frequency response spectra are intrinsic effects of finite size and discontinuous network.

It should be emphasized that proposed meta-atom not only exhibits additional attenuation pole in the upper edge band but also has a miniaturized circuit which is on the order of 65% of the CRLH atom using CSSRRP. The extended current path on the ground due to the large compression ratio of Koch curves enhances considerably the LC values of lumped elements in parallel resonant tanks of CM. Further study shows that f_{sh1} is mainly determined by external CSRRP but also affected by inner slot and interspace c between two CSSRRs, however, f_{sh2} is exclusively decided by the inner slot. This affords individual controllability over these two resonant modes.

1.4. Compact microwave device applications

1.4.1. Multiple-way and two-way Wilkinson power dividers

In this subsection, we will demonstrate the possibility of employing novel K-CSSRRP-loaded distributed CRLH TLs in the design of compact three-way fork power divider and a four-way series power divider by substituting zero phase-shift CRLH TLs for conventional 2π TLs. These artificial TLs are qualified for this task because they are readily engineered to work in balanced condition by tuning the circuit parameters. The electrically small size and the possibility to control the phase and impedance over wide ranges further facilitate this task. Although a chain of CRLH elements are more appropriate to be related as MTM TLs, the CRLH TL in current design is implemented using only one element for the sake of compactness.

Since we only have three equations regarding the balanced condition, specified phase φ and characteristic impedance Z_β, it is impossible to uniquely determine the six unknowns. Therefore, several degrees of freedom can be exploited for other requirements, e.g., miniaturization. The design procedure of an impedance transformer with φ and Z_β using distributed CRLH meta-atoms lies in four steps: (1) Select the shape and dimension of CSSRRP to roughly locate the operation frequency within the target band. Given the geometrical parameters of CSSRRP, the elements of L_P, C_P and C_k in the parallel resonant tank are determined. (2) Derive the residual three unknowns through the three available equations via a mathematical software. (3) Roughly synthesize the geometrical parameters of low-impedance patch and gap according to the newly obtained parameters. (4) Optimize the overall layout by taking into account all requirements.

Figure 20(a) depicts the schematic of the three-way fork divider. It is composed of two conventional 2π lines (in-phase power division) with characteristic impedance of Z_0 and three 90° microstrip lines with characteristic impedance of $\sqrt{3}Z_0$ which ensures an impedance match at center frequency. Here, Z_0 is the port reference impedance. We adopt the zero phase-shift CRLH atom shown in **Figure 13** to replace conventional 2π line to reduce the circuit size. Its geometrical parameters shown in the caption are cautiously designed following the design procedure. The host line length of the CRLH atom is only 9.5 mm, representing a significant

http://dx.doi.org/10.5772/65603

size reduction with regard to 76.9 mm of conventional 2π line designed on the same substrate. The host line width of the CRLH atom is deliberately chosen the same as that of 90° microstrip lines for convenience. This is applicable since CRLH atom exhibiting a wide tuning range of Z_β. For verification, the designed power divider is fabricated and measured by an *Anritsu ME7808A* vector network analyzer, see the prototype shown in **Figure 20(b)** and **(c)**. The sample occupying an area of 30 × 43 mm^2 is very compact in size, corresponding to 25.8% of the 30 × 166.4 mm^2 that its conventional counterpart occupies.

To examine the performances, **Figure 21** plots the simulated and measured *S*-parameters of the power divider. A reasonable agreement of results is observed except for slightly larger insertion loss in the measurement case. From 2.24 to 2.95 GHz, the measured return loss is better than –10 dB and the transmission losses of $|S_{21}|$ and $|S_{41}|$ suggest almost flat response around –4.98 dB. The variation of measured $|S_{31}|$ is slightly larger but within 4.77 ± 1 dB ranging from 2.28 to 2.78 GHz. At the center frequency of 2.63 GHz, an almost equal power split to all three

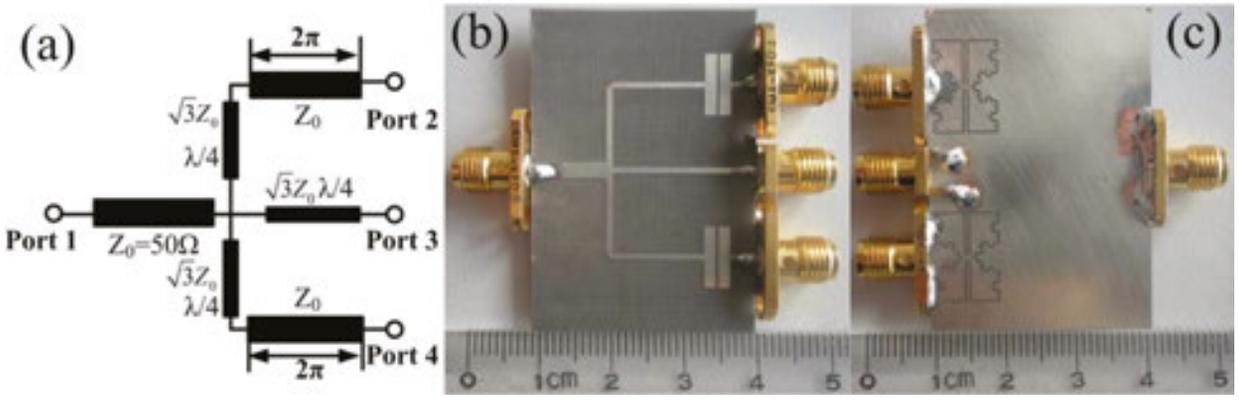

Figure 20. K-CSSRRP-loaded three-way fork power divider: (a) schematic, (b) top view, and (c) bottom view of the fabricated prototype.

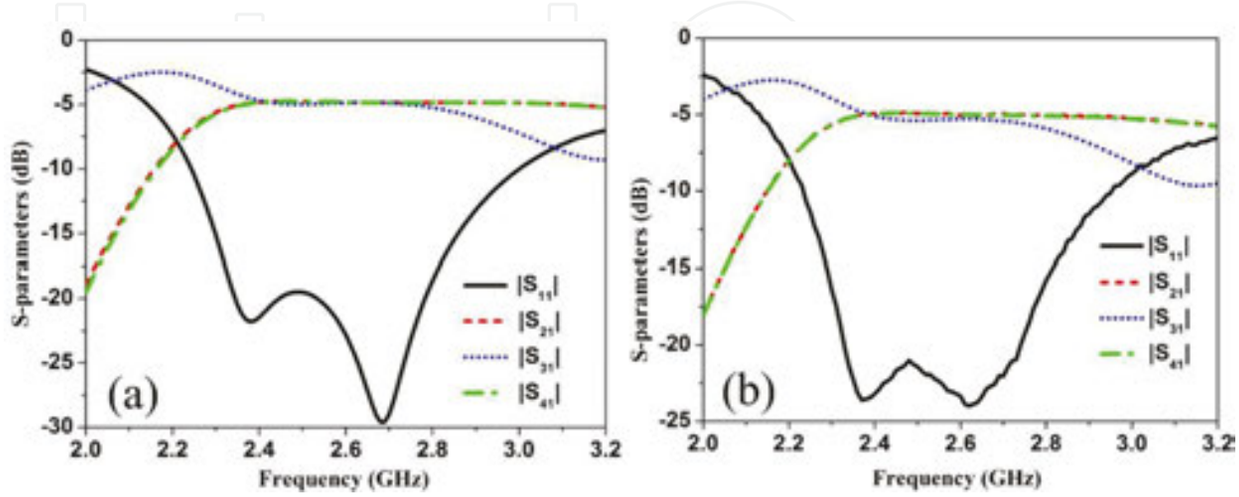

Figure 21. *S*-parameters of the three-way power divider prototype: (a) full-wave simulation and (b) measurement.

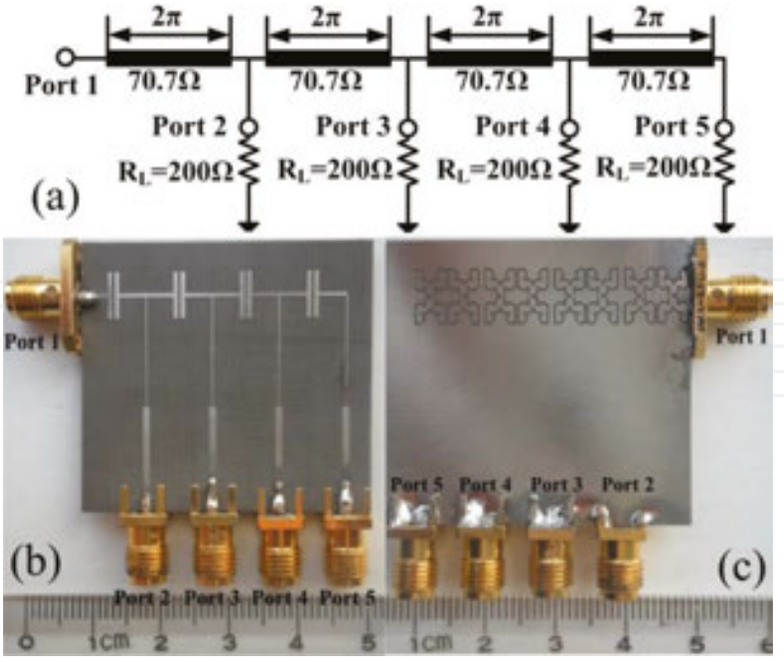

Figure 22. K-CSSRRP-loaded 1:4 series power divider: (a) schematic, (b) top view and (c) bottom view of the fabricated prototype.

output ports is observed. The slight discrepancy is possibly attributable to the radiation loss induced by the complex fractal perturbations on the ground and partially to the soldering pad which is in much proximity to the Koch slot and thus may affect the excitation of Koch slot.

For further application, a 1:4 series power divider is also designed and fabricated using the zero phase-shift CRLH atom shown in **Figure 15**. The corresponding schematic and the fabricated prototype are shown in **Figure 22**. As can be seen, the power divider consists of four series connected 2π lines for in-phase output signals. Therefore, the 1:4 power divider commonly occupies a large area especially at low frequency. Fortunately, such a 2π line can be replaced by a 0° CRLH TL due to the phase advance and the nonlinear dispersion of CRLH TL.

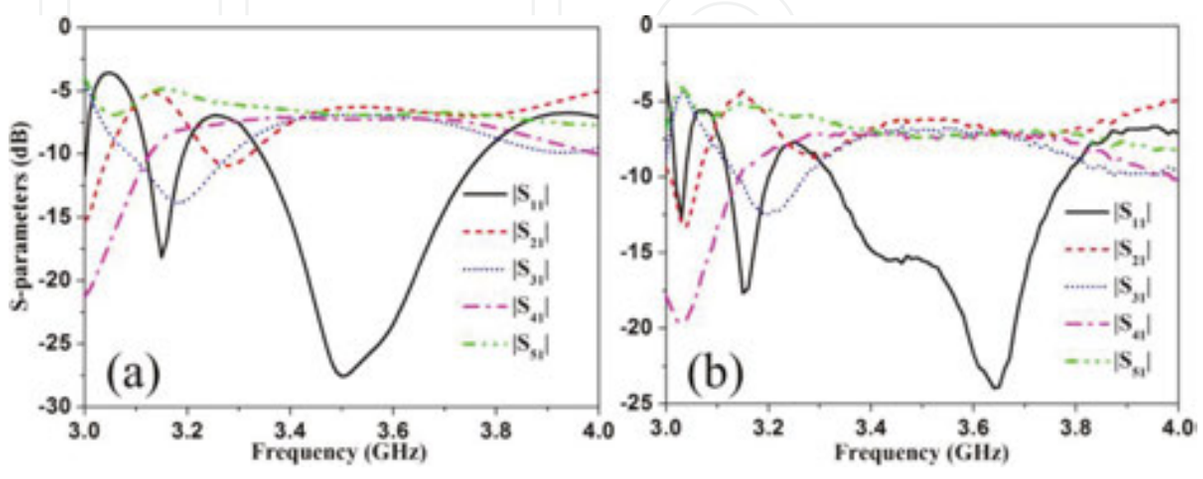

Figure 23. *S*-parameters of the proposed 1:4 series power divider: (a) simulation and (b) measurement.

http://dx.doi.org/10.5772/65603

Again, the zero phase-shift CRLH atom with detailed parameters shown in caption of **Figure 15** is synthesized following the design procedure mentioned above. For impedance matching, the characteristic impedance of 2π line or 0° CRLH TL should be $\sqrt{2}Z_0$ and the input impedance of each power split branch is 200 Ω. As such, two-staged $\lambda/4$ impedance transformers are necessary to afford a broadband impedance transformation from the required 200 Ω load impedance to 50 Ω test impedance. The narrow (15.3 × 0.16 mm^2) and wide (14.8 × 0.99 mm^2) lines function as the 158.1 Ω high-impedance transformer and the 79.1 Ω low-impedance transformer, respectively.

For verification, **Figure 23** portrays the full-wave simulated and measured *S*-parameters of our fabricated 1:4 series power divider. Satisfactory agreement of results is observed across the entire band of interest. Measurement results illustrate that return loss of the input port is better than –10 dB and the transmission power of four ports is near 7 dB. The power variation of each output port is within 5.96–8.8 dB from 3.3 to 3.8 GHz and thus the maximum variation is obtained as 2.8 dB relative to the ideal 6.02 dB. Therefore, our divider successfully fulfills the demand of equal power division. For sharp comparison, we have also fabricated and measured a 1:4 series power divider based on conventional meandered-line technique. Measured results show that the –10 dB return loss bandwidth is only 320 MHz varying from 3.38 to 3.7 GHz. Consequently, the bandwidth of our design has been broadened by 56%. Moreover, the total occupied area of our divider is only 41 × 38 mm^2 corresponding to 42% of the area 43.5 × 61.6 mm^2 that the meandered-line divider occupies.

To sum up, a novel compact resonant-type CRLH atom along with equivalent circuit model is proposed. It features inherent balance condition, additional transmission zero above the RH band and a higher degree of freedom in design over previous CSRRs-loaded counterpart. The fractal perturbation in novel CRLH atom leads to a significant shrinking of LH and RH bands and thus is of particular interest in compact device applications with a super miniaturization

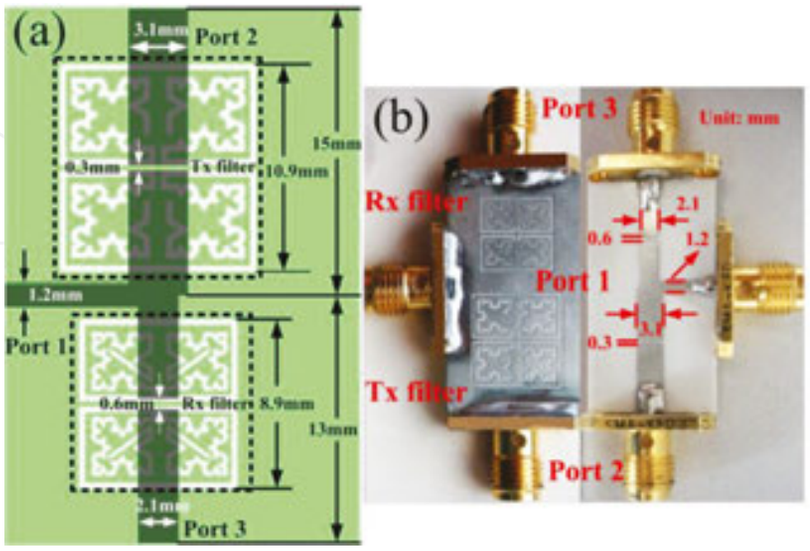

Figure 24. (a) Layout and (b) fabricated prototype of the diplexer sample. The slot width is 0.3 mm for CSSRRP while 0.2 mm for the inner slot, other geometrical parameters are: a = 4.3 mm, b = 8.3 mm, and c = 0.3 mm.

factor. The high-performance of super compact three-way and series 1:4 power divider has qualified it a good candidate.

1.4.2. Harmonic suppressed diplexer

The additional transmission zeros of CRLH atom with dual-shunt branch circuit can be directly applied to design a diplexer with harmonics suppression and enhanced frequency selectivity. A diplexer used to make receiving and transmitting share a common antenna consists of three ports, a receiver (Rx) filter and a transmitter (Tx) filter. Here, we realize both the Rx and Tx filter utilizing single K-ECSSRRP-loaded CRLH atom with specified φ and Z_β following the theory established in Section 1.3.3. The dimensions of CRLH atoms are designed and optimized to locate the Rx filter operation frequencies within GSM band centered at 1.8 GHz while Tx filter at 2.2 GHz. To ease the design, the Tx filter is directly designed from Rx filter by loading inner Koch slot of latter CRLH atom with additional stub to lower the operation frequency. Moreover, both Rx and Tx CRLH atoms are engineered to operate in balanced condition for broadband performance. For verification, the diplexer is fabricated, see **Figure 24** and measured through the *Anritsu ME7808A* vector network analyzer. The prototype occupies only 15.6 × 28 mm^2 corresponding to 0.094 λ_g × 0.168 λ_g, where λ_g is the free-space wavelength at 1.8 GHz. To the best of our knowledge, this is one of the most compact diplexers among available data.

Figure 25 illustrates the simulated and measured results of proposed diplexer. A reasonable agreement of results is observed in both cases. As shown in **Figure 25(a)**, the bandwidth of the Tx filter is measured as 220 MHz (1.61–1.83 GHz), in which the return loss $|S_{11}|$ is better than –10 dB and the insertion loss $|S_{21}|$ and $|S_{31}|$ are better than –1.5 dB. The measured bandwidth is 330 MHz (2.08–2.41 GHz) for Rx filter, where $|S_{11}|$ is better than –10 dB, $|S_{21}|$ and $|S_{31}|$ are less than –1.3 dB. Furthermore, the diplexer exhibits $|S_{11}|$= –12.9 dB, $|S_{21}|$ = –0.94 dB and $|S_{31}|$ = –14.7 dB at f_0 = 1.8 GHz, while $|S_{11}|$ = –28.1 dB, $|S_{21}|$ = –23.8 dB and $|S_{31}|$ = –0.54 dB at 2.2 GHz. The bandwidth for out-of-band suppression has been enhanced evidently which is up to 3.66 GHz characterized by $|S_{21}|$ and $|S_{31}|$ better than –20 dB. From **Figure 25(b)**, decent

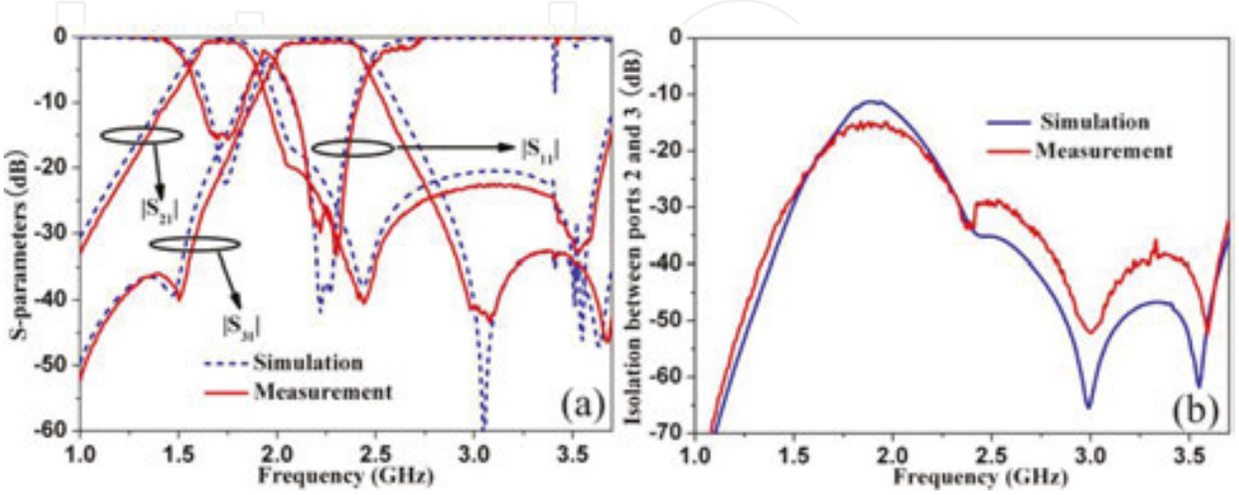

Figure 25. (a) Simulated and measured *S*-parameters and (b) isolation between output ports of proposed diplexer.

http://dx.doi.org/10.5772/65603

isolation between output ports 2 and 3 is observed. Measurement results indicate that the isolation level maintains below –15 dB up to 3.7 GHz. Slight discrepancies between simulation and measurement is attributable to the fabrication tolerances. This is especially true for the complicated CRLH atoms with zig-zag boundary. For validation, a sensitive analysis is carried out for K-ECSSRRP atom with different slot width. Numerical results suggest that the operation frequency shift upward by 1.8% while the transmission and impedance match performances are almost preserved when slot width increases by 0.1 mm. To sum up, the behavior of our diplexer fulfills unambiguously the criterion set by the wireless communication system.

In summary, the theory of dual-shunt branch circuit has been numerically studied and experimentally vilified. Due to the inherent additional transmission zero of dual-shunt branch CRLH atom, the resulting devices can be engineered with enhanced harmonic suppression and selectivity without posing penalty on circuit dimension. Moreover, the compact CRLH atom further reduces the circuit size. The high performances of designed diplexer corroborate our proposal and above statements, promising potentials in transceiver front-ends of mobile and wireless local area network (WLAN) systems.

2. Compact LH atoms for three-dimensional super lens

Three-dimensional (3D) LH-TL super lens with free-space excitation is very fascinating in practical applications since it is unnecessary to embed the sources and fields in the TL network [29, 30]. Here, we propose a 3D super lens with super resolution [31] using fractal perturbed LH TL in printed circuit board (PCB) fabrication process. The distributed LH-TL lens allows geometry scalability and avoids the parasitic RH effects in soldering the lumped elements. Due to the space-filling feature of fractals, the operation frequency in terms of subwavelength resonance is drastically lowered down. Consequently, a compact LH-TL element is engineered with large inductance and capacitance (LC) values in a limited volume.

2.1. Analysis and characterization of fractal LH-TL metamaterial

Figure 26 portrays the schematic and equivalent circuit model of the TL atom and resulting 3D lens. The TL atom with a lattice of $a \times a \times p$ consists by a metallic pattern printed on a dielectric spacer, see **Figure 26(a)**. The metallic pattern is constructed by a Sierpinski ring loaded in middle of its four concaves with four interdigitals each with a capacitance C_i. The adjacent TL atoms are interconnected through four thin meandered arms (3/2 fractal curve of first iteration order) each with an inductance L_m. Consequently, four subrings each with a self-inductance L_s are engineered. The loaded L_m and C_i contribute to the LH behavior, whereas the host medium (a combination of air gap and dielectric medium) modeled by L_0 and C_0 contribute to the RH behavior. The TL atom is isotropic since it exhibits four-fold rotational symmetry. The Sierpinski ring is designed as a fractal curve of second iteration order for the sake of compactness. In such a strategy, the inductance and capacitance (LC values) can be enhanced considerably in a limited volume, enabling the multilayered TL lens to be more appropriately described by an effective medium with homogenized μ_{eff} and ε_{eff}. By periodically arranging the fractal TL atom in *xoz*-plane and then layering the resulting structures along *y*-direction, a

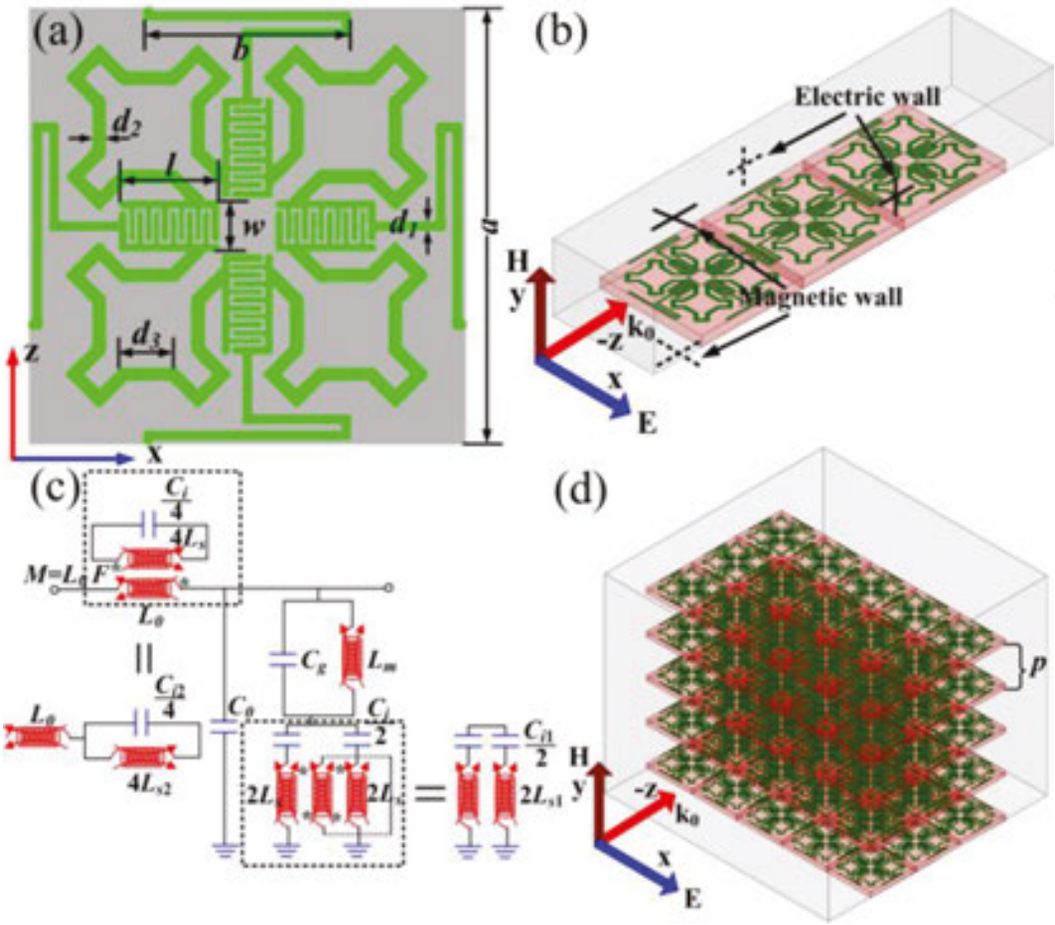

Figure 26. Topology and equivalent CM of the fully-printed LH-TL atom and lens: (a) top view and the geometrical parameter illustration of the TL atom, (b) simulation setup of an infinite slab illuminated by a plane wave of normal incidence, (c) equivalent CM, and (d) perspective view of the volumetric TL lens. The geometrical parameters (in mm) are: a = 10.6, b = 5, l = 2.4, w = 1.2, d_1 = 0.2, d_2 = 0.3, L = 6.8, and d_3 = 1.32.

3D LH-TL lens can be envisioned, see **Figure 26(d)**. It is shined by an x-polarized plane wave normally incident along z-direction. Such a configuration supports transverse electric (TE) mode with respect to xoz-plane. The computation volume is reduced to a TL atom by assigning electric and magnetic walls to four boundaries along x- and y-direction, respectively, see **Figure 26(b)**. This setup mimics an infinite array in xoy-plane.

In the model shown in **Figure 26(c)**, similar to reference [29], the fractal ring is driven by the y-oriented incident magnetic field, inducing inductive currents flowing along the interdigitals and ring which is modeled by a resonant tank formed by $4L_{s2}$ and $C_{i2}/4$ in series branch. The fractal ring couples magnetically to the host medium through a mutual inductance $M = L_0F$ which along with above resonant tank contribute the negative permeability. Here, F is the area ratio of the ring to the entire TL atom. The electric field impinging to the TL atom generates two effects which both contributing to the negative electric response. The two effects are: the oscillating current through the meandered arm and interdigital fringe modeled by a parallel tank of L_m and C_g in shunt branch; the oscillating current through the interdigitals and ring modeled by a pair of resonant tanks of $C_{i2}/2$ and $2L_{s1}/2$. The mechanism for LH behavior

http://dx.doi.org/10.5772/65603

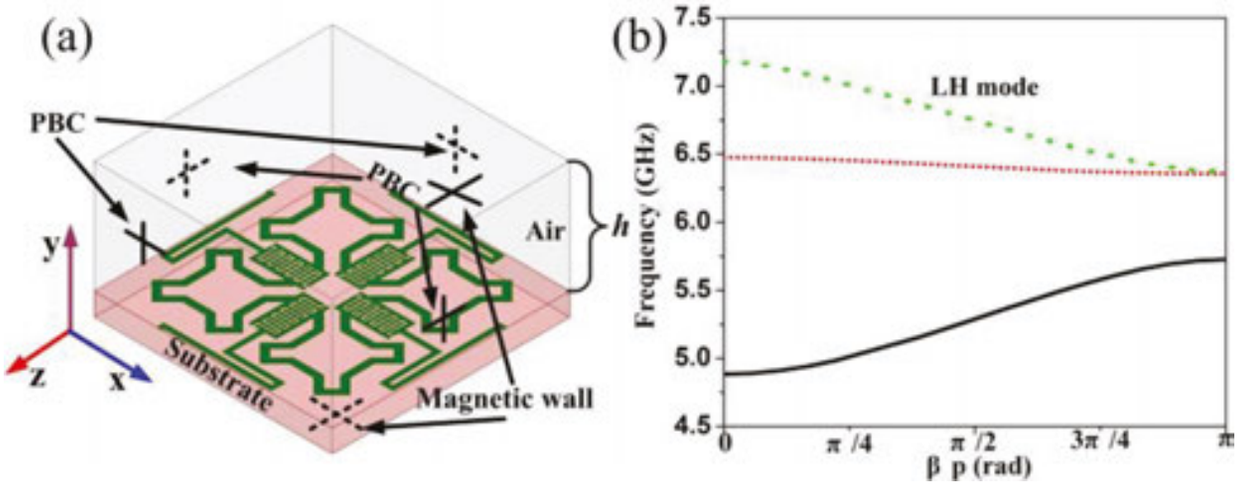

Figure 27. (a) Simulation setup for the eigenmode analysis in HFSS and (b) the dispersion curve of the TL atom for the initial design.

distinguishes from SRR-wire medium in following three aspects. First, the TL atom is physically connected to its adjacent one in coplanar structure, whereas that of SRR-wire medium is with double-layer topology. Second, the ring (magnetic response) is relevant to meandered arm (electric response) in a circuit model, whereas SRR (magnetic response) and cut wire (electric response) are independent. Most importantly, the EM wave permeating the periodically-arranged particles resembles a signal propagating along a TL, enabling low loss of resulting structure.

For characterization, the commercial full-wave finite-element-method (FEM) solver Ansoft HFSS is employed. The fractal patterns are built on 1 mm thick F4B substrate with ε_r = 2.65. The height of the air gap is h = 5 mm and thus p = 6 mm. The LH behavior can be appreciated from the dispersion data shown in **Figure 27(b)** using eigenmode simulation setup shown in **Figure 27(a)** where four walls along x- and z-directions are assigned as periodic boundary (master/slave in HFSS) while the top-and-bottom walls are assigned as magnetic walls. As expected, the backward wave dispersion (negative slope) is clearly observed from 6.37 to 7.18 GHz with a fractional bandwidth of 12%.

2.2. Design and realization of super lens

Now, we show how to design the basic TL atom and resulting super lens. To lay a solid theoretical method for implementation of $Z = Z_0$ and $n_{\text{eff}} = -1$ which are necessary for super lens, we derive constitutive effective parameters for the 3D layered lens from CM. According to Floquet-Bloch theory, the phase shift φ per cell and the Bloch impedance Z_β can be calculated as

$$\cos\varphi = \cos(\beta p) = 1 + Z_s(j\omega)Y_p(j\omega)/2 \tag{35}$$

$$Z_\beta = \sqrt{Z_s(j\omega)[Z_s(j\omega)/4 + 1/Y_p(j\omega)]} \tag{36}$$

where $Z_s(j\omega)$ and $Y_p(j\omega)$ are the impedance and admittance of the series and shunt branch, respectively and are associated with the effective material parameters as

$$Z_{\mathrm{s}}(j\omega) = j\omega\mu_{\mathrm{eff}}\mu_0 = j\omega L_0 + \frac{1}{\frac{1}{j4\omega L_{\mathrm{s2}}} + \frac{j\omega C_{\mathrm{i2}}}{4}} \tag{37}$$

$$Y_{\mathrm{p}}(j\omega) = j\omega\varepsilon_{\mathrm{eff}}\varepsilon_0 = j\omega C_0 + \frac{1}{\frac{1}{j\omega C_{\mathrm{g}} + \frac{1}{j\omega L_{\mathrm{m}}}} + \frac{1}{j\omega C_{\mathrm{i1}}} + j\omega L_{\mathrm{s1}}} \tag{38}$$

Here, L_{r1}, C_{r1}, L_{r2} and C_{r2} are the equivalent inductances and capacitances by taking the coupling effects into consideration and are associated with L_r and C_r as

$$4L_{\mathrm{s1}} = L_{\mathrm{s}} - \mathrm{M}^2/L_0,\ 4L_{\mathrm{s2}} = \frac{\mathrm{M}^2}{4L_{\mathrm{s}}},\ C_{\mathrm{i1}} = C_{\mathrm{i}},\ C_{\mathrm{i2}} = \frac{4L_{\mathrm{s}}^2 C_{\mathrm{i}}}{\mathrm{M}^2} \tag{39}$$

Insertion of Eq. (39) into Eqs. (37) and (38) yields immediately the effective material parameters

$$\mu_{\mathrm{eff}} = 1 + \frac{C_{\mathrm{i}}M^2}{4L_0}\frac{\omega_{\mathrm{r2}}^2}{(1-\omega^2/\omega_{\mathrm{r2}}^2)} \tag{40a}$$

$$\varepsilon_{\mathrm{eff}} = 1 + \frac{C_{\mathrm{i}}}{C_0}\frac{(1-\omega^2/\omega_{\mathrm{g}}^2)}{(1-\omega^2/\omega_{\mathrm{r1}}^2)(1-\omega^2/\omega_{\mathrm{g}}^2) - \omega^2/\omega_{\mathrm{m}}^2} \tag{40b}$$

where ω_{r1}, ω_{r2}, ω_g and ω_m are

$$\omega_{\mathrm{r1}}^2 = \frac{1}{(L_{\mathrm{s}} - \mathrm{M}^2/L_0)C_{\mathrm{i}}},\ \omega_{\mathrm{r2}}^2 = \frac{1}{L_{\mathrm{s}}C_{\mathrm{i}}},\ \omega_{\mathrm{g}}^2 = \frac{1}{L_{\mathrm{m}}C_{\mathrm{g}}},\ \omega_{\mathrm{m}}^2 = \frac{4}{L_{\mathrm{m}}C_{\mathrm{i}}} \tag{41}$$

The effective permittivity and permeability tensors of the TL lens can be written as

$$\varepsilon(\omega) = \varepsilon_0\begin{pmatrix} \varepsilon_{\mathrm{eff}} & 0 & 0 \\ 0 & \varepsilon_{\mathrm{avg}} & 0 \\ 0 & 0 & \varepsilon_{\mathrm{eff}} \end{pmatrix}, \mu(\omega) = \mu_0\begin{pmatrix} 1 & 0 & 0 \\ 0 & \mu_{\mathrm{eff}} & 0 \\ 0 & 0 & 1 \end{pmatrix}, \tag{42}$$

where $\varepsilon_{\mathrm{avg}}$ represents the averaged permittivity of the host medium. Insertion of $M = L_0F$ into Eq. (39), we conclude that L_{s1} is inversely proportional to L_0. Therefore, the electric resonance is proportional to L_0. Moreover, Eq. (40) suggests that the air gap plays an important role in affecting the constitutive parameters and the effective impedance while Eq. (41) indicates that L_{m}, L_{s} and C_{i} can be utilized to control the electric and magnetic resonances.

With above fundamentals known, we designed a 3D TL super lens working at f_0 = 5.35 GHz with optimized geometrical parameters shown in caption of **Figure 26**. The commercially available 3 mm-thick FR4 substrate with ε_r = 4.2 is selected in the super-lens design. The air space is selected as h = 9 mm to guarantee good impedance matching of the lens to free space. **Figure 28** depicts the dispersion diagram and *S*-parameters of designed TL atom which will be utilized as a building block for super lens. From **Figure 28(a)**, the backward LH band ranges

http://dx.doi.org/10.5772/65603

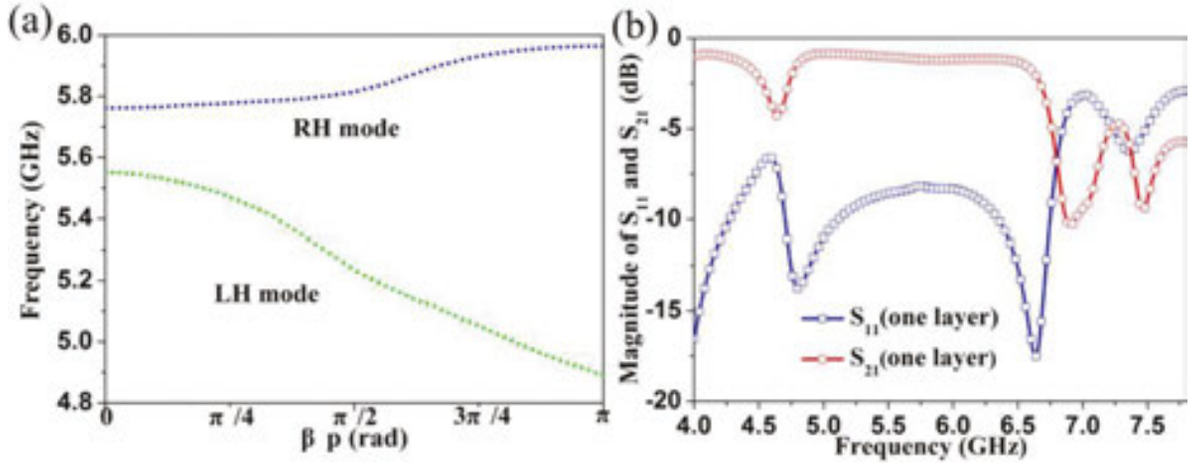

Figure 28. (a) Dispersion diagram and (b) simulated *S* parameters against frequency of designed TL atom.

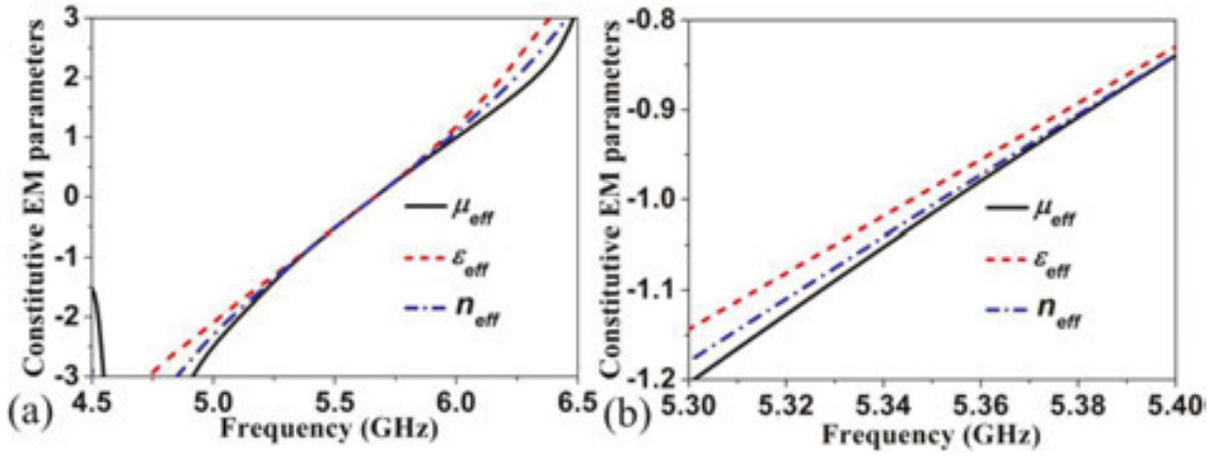

Figure 29. Constitutive EM parameters (real parts) extracted from simulated *S*-parameters: (a) overall view and (b) zoom-in view around f_0 = 5.35 GHz.

from 4.89 to 5.55 GHz, corresponding to a fractional bandwidth of 12.6%. The element size is evaluated as $\lambda_0/5.3 \times \lambda_0/5.3$ at 5.35 GHz which is within the limit of an effective medium ($\lambda_0/4$). The βp is on the order of 70°, yielding a refractive index of $n = -1.028$ according to $n = c\beta/\omega a$. Moreover, the RH band with positive negative index follows the LH band though a narrow interval of 5.55–5.76 GHz. This narrow signal inhibition does not lead to notable stop band in **Figure 28(b)** but induces slightly large insertion loss and weak ripple in S_{11} around 5.74 GHz. It enhances with increased element number in propagation direction and thus an obvious stop band would emerge when more TL atoms are cascaded. The insertion loss retains at a decent level in the pass band.

As shown in **Figure 29**, the effective parameters are retrieved as $\mu_{\text{eff}} = -1.006 - j0.132$, $\varepsilon_{\text{eff}} = -0.995 + j0.049$ and $n = -1.004 - j0.041$ at f_0 = 5.35 GHz under time-harmonic progression $e^{j\omega t}$. The refractive index is in excellent agreement with that calculated from dispersion diagram shown in **Figure 28(a)**. Therefore, the condition for Veselago-Pendry lens which require simultaneously good impedance matching ($\mu_{\text{eff}} = \varepsilon_{\text{eff}} = -1$) and $n = -1$ is successfully fulfilled.

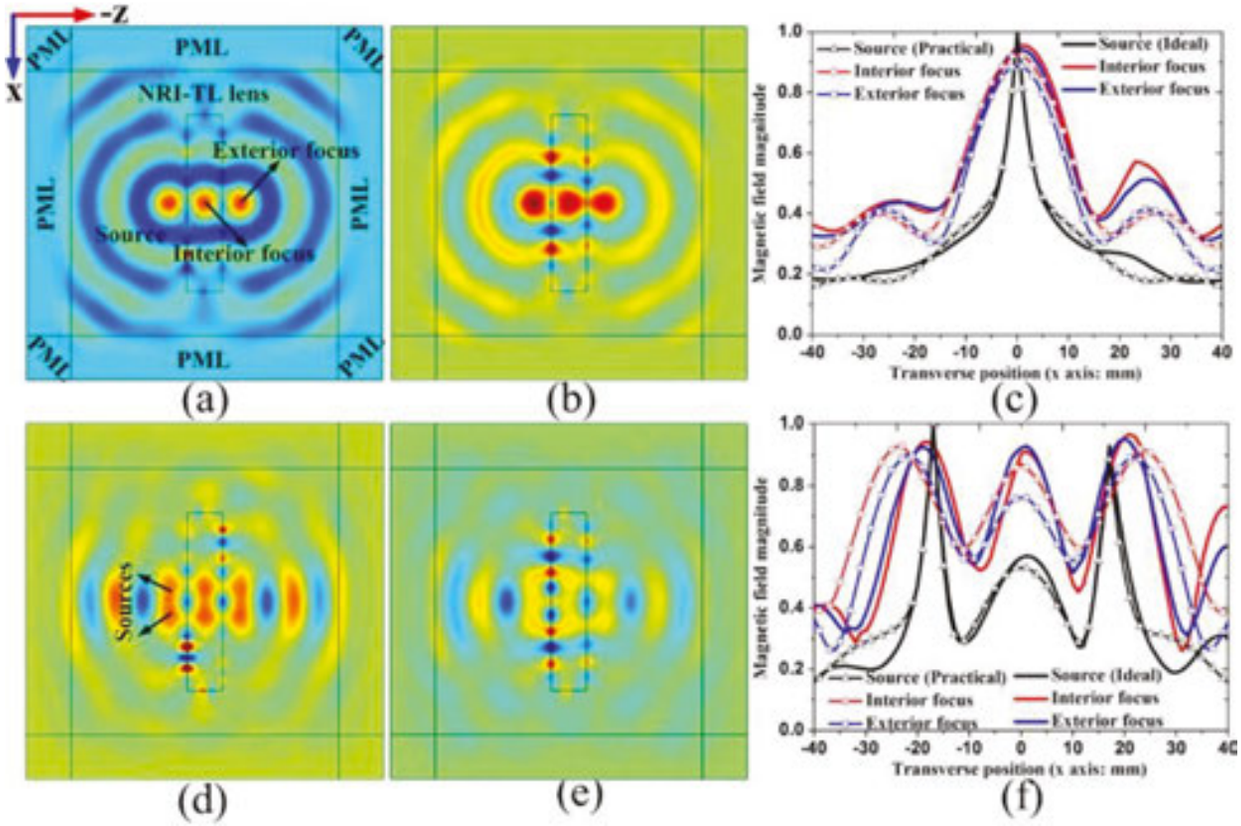

Figure 30. Numerically simulated magnetic field distributions of the designed TL lens. Field distributions for (a and d) ideal lens with $\mu_y = \varepsilon_x = -1$ and (b and e) designed (practical) lens with $\mu_y = -1.006 - j0.132$, and $\varepsilon_x = -0.995 + j0.049$ in (a–c) single-source and (d and e) dual-source case. (c and f) The field curve plotted along x-axis at the center of the lens.

2.2. Numerical and experimental results

To verify the subwavelength focusing, we numerically designed a TL lens using the extracted effective parameters. The simulation is conducted in Comsol Multiphysics™ software package, where a current source oriented along y-axis is placed in front of the TL lens with an overall size of 200 × 40 mm^2 to generate EM wave propagating along z-direction. A sufficiently large PML boundary with a total area of 400 × 400 mm^2 is employed to encompass the lens and the source. **Figure 30** portrays the magnetic field distribution within the entire calculation domain. For comprehensive study, two cases are considered for both designed (practical) lens and ideal lens with $\mu_y = -1$ and $\varepsilon_x = -1$, i.e., single source and dual closely arranged identical sources with an interval of 34 mm.

Obvious focusing behavior is clearly suggested inside (interior focusing) and in front (exterior focusing) of the lens for both designed and ideal lens in either single-source or dual-source case. The evanescent wave amplification is clearly observed along the two-slab interfaces. The large field concentration on interfaces is attributable to plasmonic surface waves at the interface of LH and RH media. The nonideal material parameters away from –1 induce slightly asymmetric fields, discontinuous wave front and lower imaging intensity observed in practical lens due to slight loss and impedance mismatch at the interface of lens and free space. Nevertheless, the loss originated from imaginary parts of μ_{eff} and ε_{eff} do not pose critical

http://dx.doi.org/10.5772/65603

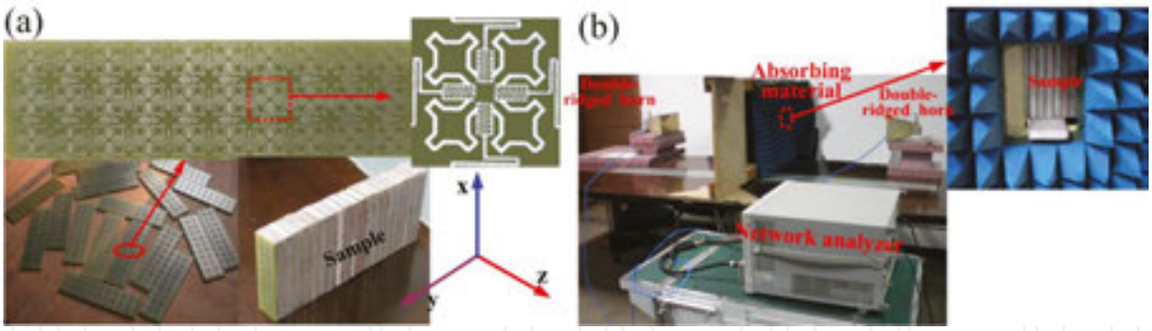

Figure 31. (a) Photograph of the fabricated TL lens and (b) free-space measurement system for *S*-parameters.

influence on focusing. The clearly converged spots for dual-source practical lens give strong support to above statement, which should be emphasized. The size of converged images measured by 3 dB contour (half-power beam width, HPBW) is about 19 mm, corresponding to 0.34 λ_0 at 5.35 GHz. Therefore, the subwavelength imaging is unambiguously validated beyond the diffraction limit with both focused propagating wave and amplified evanescent wave. The spot size characterized by HPBW in the dual-source case is observed slightly narrower than that in single-source case. This is attributable to the wave interference of the two sources.

For verification, the designed TL lens is fabricated and measured, see **Figure 31(a)**. In fabrication, a total of 10 × 3 TL atoms are fabricated on FR4 substrate board using standard PCB technology. To sustain the bulk TL lens with desired air spacer, each substrate board is supported by a plastic foam of identical size with $\varepsilon_{foam} = 1.2$ and $h = 9$ mm. Then, 20 substrates and 20 plastic foams are alternatively stacked by adhesives and are reinforced by a hot press to form a lens occupying a volume of 106 × 240 × 31.8 mm^3. To guarantee axial magnetic excitation, two small loop antennas each with an inner diameter of 4.6 mm are implemented in shielded-loop configuration to mitigate unbalanced currents.

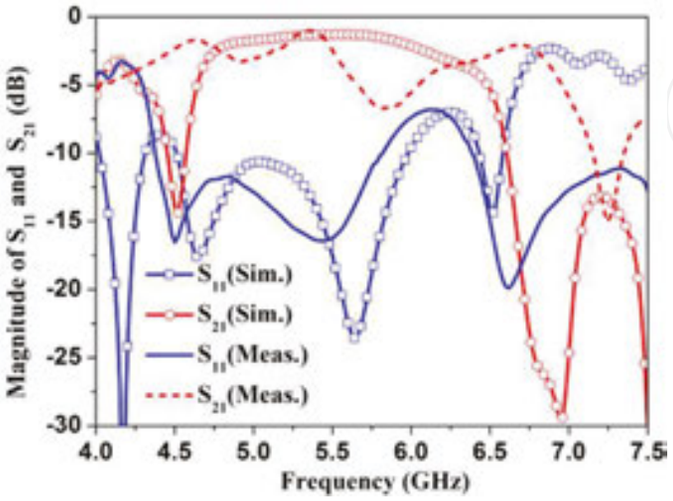

Figure 32. Simulated and measured *S*-parameters of the TL lens.

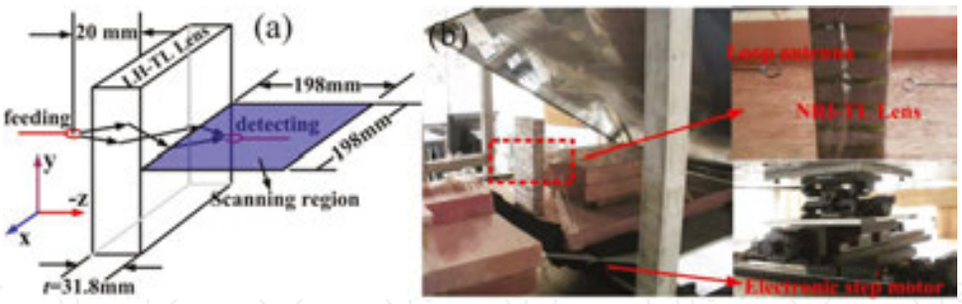

Figure 33. (a) Schematic illustration and (b) near-field measurement system of the free-space focusing apparatus.

The *S*-parameters of the lens are measured utilizing the setup shown in **Figure 31(b)**. Two double-ridged horn antennas functioning as the receiver and transmitter, respectively, are placed at two sides of the sample, each is 90 mm away from the center sample to provide a plane EM wave with required polarization. The sample is placed in a drilled aperture on a sufficiently large wooden board aside which a mass of absorbing materials were used to block diffracted energy. As shown in **Figure 32**, numerical and experimental *S*-parameters coincide reasonably except for a transmission dip around 5.75 GHz and blue shifted signal inhibition band at high frequencies in measurement case. The mutual coupling between adjacent atoms in longitudinal direction gives rise to wider pass band. Moreover, the nonideal foams with $\varepsilon \neq 1$ in experiments and infinite dimension in *xoy*-plane in simulations also give rise to the discrepancy. Nevertheless, these factors play a negligible role in degrading the electrical performances at 5.35 GHz where the focusing performance will be evaluated. The simulated (measured) return loss is observed as –13.1 (–15.9 dB) at this point, implying a good impedance matching to free space.

For dual-source imaging, additional power-division circuit is necessary and wave interference of two closely distributed sources may degrade the focusing quality in terms of weak field intensity at focal point. Here, we only performed experiments for single-source imaging by measuring magnetic field intensity using loop antenna, see setup shown in **Figure 33**. The transmitting loop antenna (20 mm away from the slab), is stationary and illuminates at the front side of the lens (slightly larger than $t/2$) while the detecting loop antenna scans a region of 198 × 198 mm^2 at rear side of the sample by an electronic step motor. **Figure 34** plots the measured magnetic field intensity and phase distribution in steps of 1 mm at rear side (focal region) of the lens at three different frequencies. Here, the field intensity has been normalized to their maximum amplitude. From **Figure 34(a)** and **(b)**, the well-resolved imaging can be evidenced from both localized field intensity and reversal of smooth concave phase fronts near the focal plane at 5.35 and 5.4 GHz. The HPBW indicated by –3 dB intensity (along *y*-axis) is measured about 21.9 mm (0.39 λ_0) which is in reasonable agreement with that obtained in simulations. The slightly deteriorative spot size may be attributable to the adhesives employed in experiments which also introduce additional loss. Therefore, significant resolution improvement is achieved with respect to the 0.55 λ_0 [30], which suggests that the imaging resolution in this approach is less susceptible to the loss than that in other approaches. However, there is none evidence for subwavelength focusing from magnitude or phase plotted in **Figure 34(c)**, where the transverse size of elongated

http://dx.doi.org/10.5772/65603

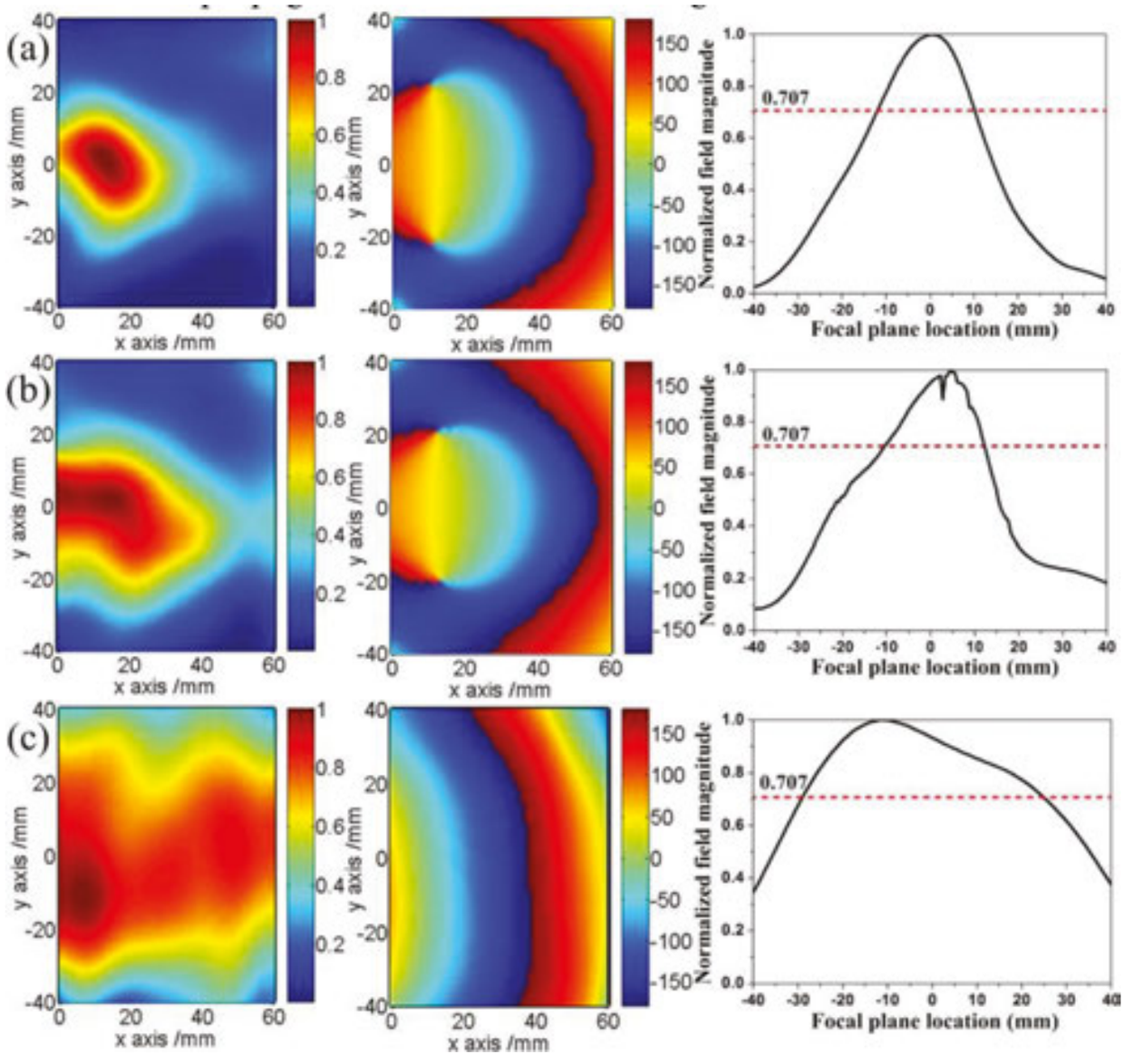

Figure 34. Measured results at rear side of the volumetric TL lens at: (a) 5.35, (b) 5.4, and (c) 6.7 GHz. The left, middle, and right columns are normalized magnetic field intensity, phase distribution and –3 dB contour at the focal plane.

pattern measured by –3 dB contour is more than 55 mm near above focal region and the convex phase front occurs all time, indicating a plane-wave like propagation at 6.7 GHz in RH region.

3. Compact meta-atoms for superscatterer illusions devices

In this section, we conceptually proposed and experimentally demonstrated a superscatterer illusion device [32] with abundant functionality inspired by the concept of magnifying lenses [33, 34] using transformation optics (TO) theory. A new strategy to miniaturize the meta-atom

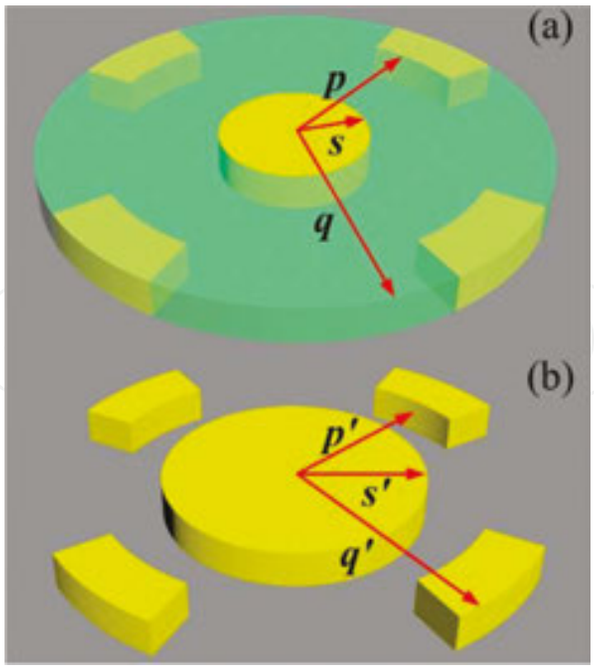

Figure 35. Scheme of the proposed superscatterer illusion device: (a) the original metallic object (yellow) is wrapped by the illusion device (light green) and (b) the virtual enlarged metallic object at the original center with four wing dielectric objects.

is proposed by combining both electric and magnetic particles. Using such a compact building block, a proof-of-concept sample consisted by 6408 gradually varying meta-atoms is designed, fabricated and measured.

3.1. Scheme and theoretical design

The device which tightly wraps an original metallic object (denoted as yellow) in actual space, see **Figure 35(a)**, is a shell (denoted as light green) embedded by four symmetrically located wing objects (denoted as light yellow). It functions to transform the metallic object into multiple isolated ghost objects with isotropic material properties ($\overline{\overline{\varepsilon}}' = \varepsilon_r \bar{I}, \overline{\overline{\mu}}' = \mu_r \bar{I}$) and an enlarged metallic object at center in virtual space, see **Figure 35(b)**. In other words, the functional device enables the radar scattering signature of a metallic object to equal that of an enlarged metallic object and four symmetrically arranged ghost objects under EM wave illumination. The proposed scheme with complex and versatile functionality inherits the merits of both superscatterers and cognitive deception and is not confined to metallic objects but also suitable for dielectric objects.

In actual space, the radius of the object (also the inner radius of the ghost device), the inner and outer wings are denoted as s, p and q (also the outer radius of the device), respectively, whereas they are s', p' and q' in virtual space. To ease the design, we choose $p = p'$, $q = q'$ and assume that the material property and geometrical layout of the four wing objects are the same. The anistropic and inhomogenious material parameters of the shell (region I) and wings (region II) are different and require precise design based on the TO theory. We remark the number of

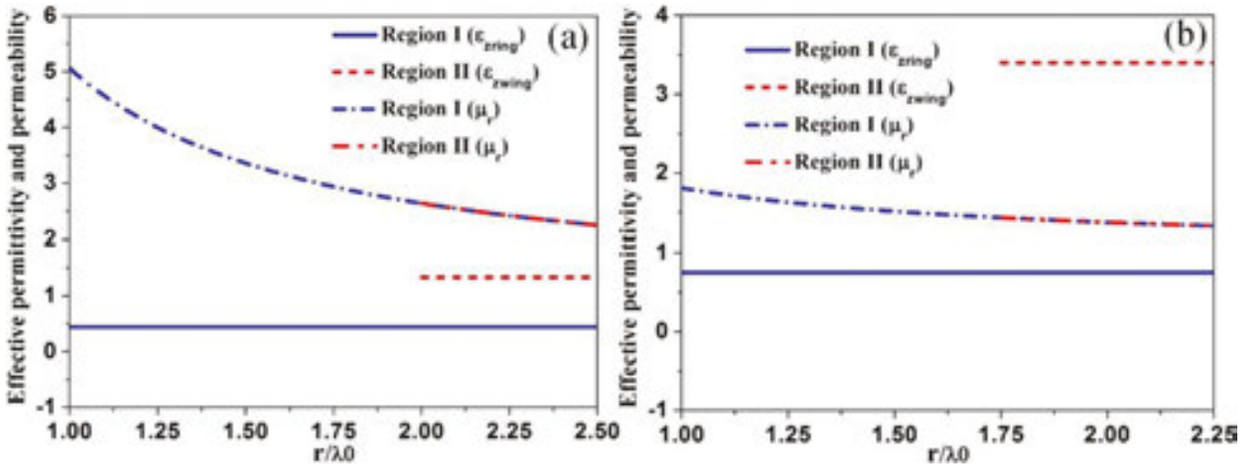

Figure 36. Theoretically calculated material profiles as a function of normalized radius in region I and region II which has been normalized to the free-space working wavelength $\lambda_0 = 30$ mm: (a) case 1: $\varepsilon_{\text{virtual}} = 3$, $s = \lambda_0$, $= 1.5\lambda_0$, $p = p' = 2\lambda_0$, and $q = q' = 2.5\lambda_0$ and (b) Case 2: $\varepsilon_{\text{virtual}} = 4.53$, $s = \lambda_0$, $s' = 7/6\lambda_0$, $p = p' = 1.75\lambda_0$, and $q = q' = 2.25\lambda_0$.

wings can be arbitrary engineered provided that the required complex material profiles can be realized by metamaterials and in this work four wings each separated by 90° are selected with four-fold rotational symmetry. Moreover, the material properties of the virtual wing object can also be arbitrarily predesigned. Here, we tailor the wing property only by tuning the dielectric constant $\varepsilon'_{\text{virtual}}$ since most materials in nature are nonmagnetic.

We derived the required material parameters in region I and II through a general transformation $r = f(r')$ in 3D spherical coordinate (r, φ, θ). According to TO theory, the diagonal permittivity tensor $\overline{\overline{\varepsilon}}$ and permeability tensor $\overline{\overline{\mu}}$ in physical space associate with $\overline{\overline{\varepsilon'}}$ and $\overline{\overline{\mu'}}$ in virtual space as $\overline{\overline{\varepsilon}} = \Lambda\overline{\overline{\varepsilon'}}\Lambda^T/|\Lambda|$ and $\overline{\overline{\mu}} = \Lambda\overline{\overline{\mu'}}\Lambda^T/|\Lambda|$. Here, $\Lambda_{ij} = \partial x_i/\partial x_j^{/}$ is the Jacobian matrix of the transformation and $|\Lambda|$ is its determinant. After some derivations, the permittivity tensor with similar form as the permeability tensor is obtained as

$$\overline{\overline{\varepsilon}}(r,\varphi,\theta) = \begin{bmatrix} \dfrac{f'(r')r'^2\varepsilon'_r}{f(r')^2} & 0 & 0 \\ 0 & \dfrac{\varepsilon'_\varphi}{f'(r')} & 0 \\ 0 & 0 & \dfrac{\varepsilon'_\theta}{f'(r')} \end{bmatrix} \tag{43}$$

In this particular design, the proposed superscatterer illusion functionality can be readily realized through following transformation:

$$(r \quad \varphi \quad \theta) = \left(k(r'-s') + s \quad \varphi' \quad \theta'\right) \tag{44}$$

where $k = (q-s)/(q-s')$ is a constant related to the magnifying factor that can be arbitrarily designed. By substituting Eq. (44) into Eq. (43), we immediately obtain the required permittivity or permeability tensor as

$$\overline{\overline{\varepsilon}}(r,\varphi,\theta) = \begin{bmatrix} \dfrac{(r-s+ks')^2\varepsilon'_r}{kr^2} & 0 & 0 \\ 0 & \dfrac{\varepsilon'_\varphi}{k} & 0 \\ 0 & 0 & \dfrac{\varepsilon'_\theta}{k} \end{bmatrix} \tag{45}$$

For 2D illusion device in the cylindrical coordinates (r, φ, z), see cross-section shown in **Figure 35**, the full diagonal parameter tensors (μ_r, μ_φ, μ_z) and (ε_r, ε_φ, ε_z) in regions I and II have the same form as those in the spherical 3D case. Since all cases considered in this work are transverse-electric (TE) wave excitation with z-polarization, the full diagonal-parameter tensors for proposed EM functionality can be simplified to three permittivity and permeability components (μ_r, μ_φ, ε_z) for an easy design [35]

$$\begin{pmatrix} \mu_r & \mu_\varphi & \varepsilon_{z\text{wing}} \end{pmatrix} = \begin{pmatrix} \dfrac{f'(r')^2 r'^2}{f(r')^2} & 1 & \dfrac{\varepsilon'_{\text{virtual}}}{f'(r')^2} \end{pmatrix} \tag{46a}$$

$$\begin{pmatrix} \mu_r & \mu_\varphi & \varepsilon_{z\text{ring}} \end{pmatrix} = \begin{pmatrix} \dfrac{f'(r')^2 r'^2}{f(r')^2} & 1 & \dfrac{1}{f'(r')^2} \end{pmatrix} \tag{46b}$$

where $\varepsilon_{z\text{ring}}$ and $\varepsilon_{z\text{wing}}$ are z-directed permittivity components in region I and II, respectively.

The superscatterer illusion device is designed to work around 10 GHz in X band. **Figure 36** portrays the required anisotropic and inhomogeneous material profile as a function of radius in both regions. Without loss of generality, two illusion devices with large and smaller magnifying factor of $s'/s = 1.5$ and $s'/s = 1.167$ are considered. From **Figure 36**, it is learned that the radial permeability μ_r exhibits an anomalous negative dispersion in both regions, whereas μ_r has a positive slope for a shrinking device [35]. Moreover, μ_r increases drastically and thus exhibits a sharper slope while ε_z presents an inverse manner with respect to μ_r when s' increases or s and q decrease. Notice that the sensitivity of q on the material property is more mitigative than that of s and s'. In Case 1, the material parameters is $\varepsilon_{z\text{ring}}$= 0.444 and $2.25 \le \mu_r \le 5.06$ in region I ($\lambda_0 \le r \le 2.5\ \lambda_0$) while they are $\varepsilon_{z\text{wing}}$= 1.333 and $2.25 \le \mu_r \le 2.64$ in region II ($2\lambda_0 \le r \le 2.5\ \lambda_0$). In Case 2, they are $\varepsilon_{z\text{ring}}$ = 0.75 and $1.33 \le \mu_r \le 1.812$ in region I ($\lambda_0 \le r \le 2.25\ \lambda_0$) while $\varepsilon_{z\text{wing}}$= 3.34 and $1.33 \le \mu_r \le 1.435$ in region II ($1.75\ \lambda_0 \le r \le 2.25\ \lambda_0$). In practice, there is no size limitation on our superscatterer device which can be engineered substantially larger to deceive any sized object. However, it is engineered relatively small in this design for experimental convenience due to scanning capability limit of available near-field measurement system.

3.2. Metamaterial design and device fabrication

The above required gradient material profiles in both regions can be realized using compact meta-atoms. Since it is easy to fully cover a small scope of permeability using only one type of subwavelength elements, we consider implementing the superscatterer illusion in Case 2 with more relaxed slope of μ_r. **Figure 37** depicts the topology and fabricated prototype of designed illusion device. Here, a new strategy is proposed to simultaneously fulfill the less-than-unity

http://dx.doi.org/10.5772/65603

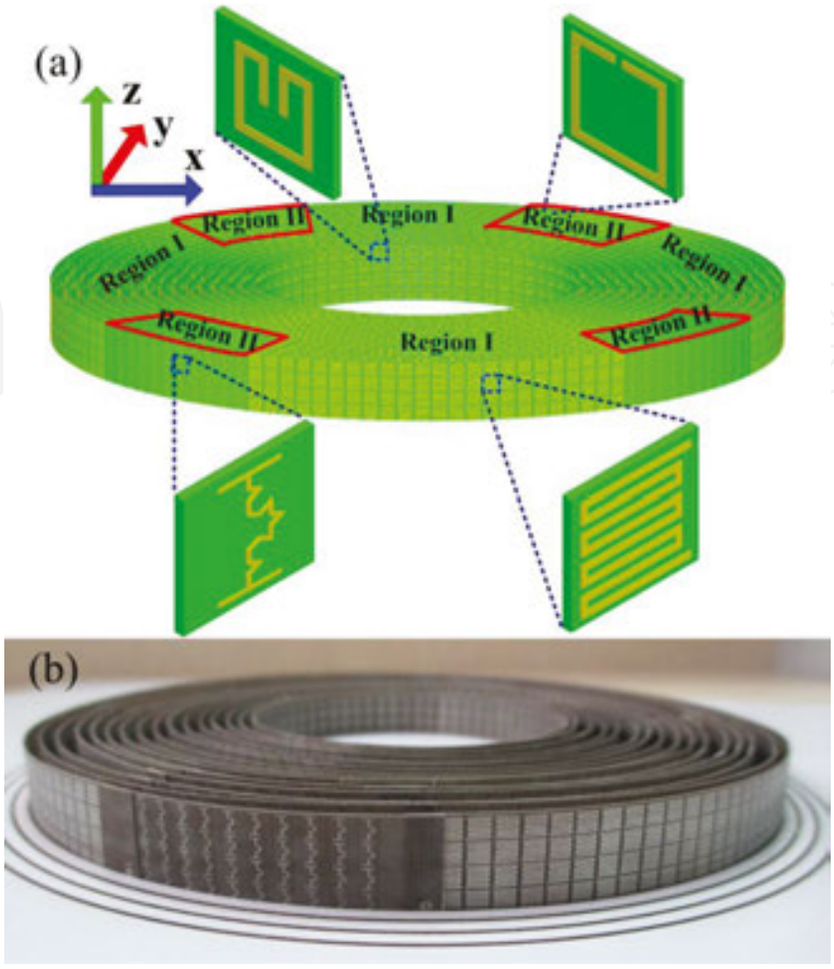

Figure 37. (a) Topology and (b) fabricated prototype of the proposed superscatterer illusion device, which is composed of four types of subwavelength electric and magnetic particles.

permittivity ε_z while the larger-than-unity permeability μ_r. Two kinds of meta-atoms each composed of an electric resonator and a magnetic inclusion are designed on both sides of a 0.2 mm-thick flexible F4B board with ε_r= 2.65, see **Figure 37(a)**. Through a proper design, the working frequency can be precisely engineered above the electric plasma frequency ω_p while below the magnetic resonance. In region I, the meta-atom consists of a meander line electric resonator and a split-ring resonator (SRR) with two concave arms; whereas in region II the meta-atom consists by SRR and Koch-shaped cut-wire resonator. Two factors give rise to the meta-atom miniaturization within a limited volume: meandered or fractal strategy for electric resonator design and layered coupling between layered electric and magnetic particles. In this regard, the volumetric devices made of these meta-atoms are more feasible to be described by an effective medium and thus the collective EM response is less affected by the parasitic diffractions, enabling an exact design due to good approximation of an infinite array to a finite bulk medium. Moreover, the low loss and relaxed material parameter dispersion enable desirable performance and working bandwidth of the superscatterer illusion device since the meta-atoms operate at nonresonance region.

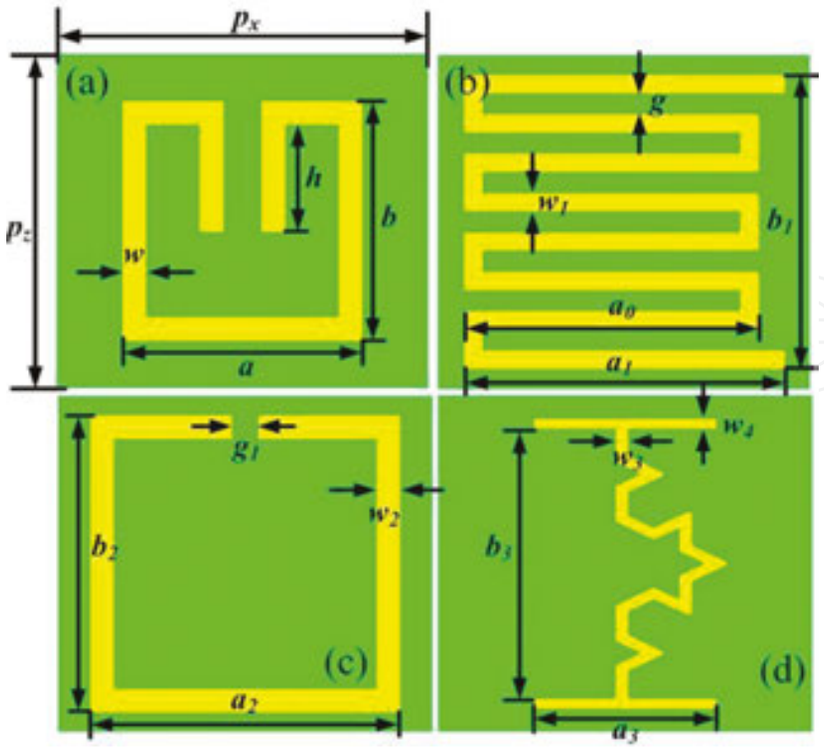

Figure 38. The illustration of physical parameters of four electric and magnetic particles. "(a)SRR with two concave arms. (b) Meanderline electric resonator." behind the word "particles.(c) conventional SRR. (d)Koch-shaped cut-wire resonator."

In the fabricated prototype, the superscatterer illusion device is discretized into a total of 6408 grids (meta-atoms) each occupying an area of $p_r \times p_\varphi \times p_z = 2.5 \times 3 \times 2.7\ \text{mm}^3$ ($0.083\ \lambda_0 \times 0.1\ \lambda_0 \times 0.09\ \lambda_0$). This size level goes beyond the shrinking illusion device [35] in terms of effective medium and homogenization. The prototype is synthesized by 16 concentric layers each owning one or two particles of different geometrical parameters and composed of four meta-atoms along z-direction, corresponding to a height of 10.8 mm ($0.36\ \lambda_0$). The 2.5 mm interval between neighboring layers is guaranteed by adhering the 16 flexible boards to 0.2 mm-wide concentric circular rabbets carved on a hard-foam board by the LPKF milling machine. The shell extends from the 1st to 16th layer and contains a sum of 5288 elements, whereas the four-wing objects extend from the 10th to 16th layer and consist by 1120 particles. A total of 22 groups of different geometrical parameters of meta-atoms, see **Figure 38** and **Table 4**, are finely optimized in Ansoft HFSS to generate the required permittivity and permeability.

In the simulation setup shown in **Figure 39(a)**, z-polarized EM wave is incident parallel to the dielectric board with magnetic fields penetrating through the magnetic inclusions along the x-direction (radial direction in cylindrical coordinates). To mimic an infinite array, four transverse walls are assigned master/slave boundary in HFSS while the two walls along propagation direction are assigned the Floquet ports. From **Figure 39(b)** and **(c)**, it is learned that the operation frequency of both meta-atoms locates precisely above ω_p of the electric resonator while below resonance of the magnetic inclusion. The material parameters are

	Region I			Region II					
Number of Layers	***H* [mm]**	ε_z	μ_r	w_3 **[mm]**	a_3 **[mm]**	g_1 **[mm]**	a_2 **[mm]**	ε_z	μ_r
1	0.9	0.7328	1.807						
2	0.87	0.7459	1.745						
3	0.835	0.7362	1.679						
4	0.8	0.7451	1.621						
5	0.77	0.7383	1.583						
6	0.74	0.7376	1.548						
7	0.71	0.7331	1.515						
8	0.68	0.7387	1.485						
9	0.655	0.7395	1.461						
10	0.633	0.746	1.429	0.108	1.548	0.11	2.5	3.395	1.441
11	0.61	0.7382	1.417	0.108	1.548	0.13	2.5	3.405	1.416
12	0.59	0.7418	1.395	0.105	1.4	0.2	2.6	3.396	1.394
13	0.56	0.7391	1.371	0.105	1.47	0.15	2.5	3.392	1.378
14	0.54	0.7402	1.36	0.102	1.462	0.17	2.5	3.397	1.358
15	0.51	0.745	1.342	0.111	1.48	0.2	2.5	3.405	1.34
16	0.49	0.7413	1.33	0.105	1.435	0.2	2.5	3.393	1.334

Note: The other geometrical parameters are given as follows: p_z = 2.7mm, p_x = 3 mm, $a = b$ = 1.95 mm, w = 0.2 mm, a_1 = 2.607mm, $b_1 = a_0$ = 2.394 mm, $w_1 = g$ = 0.16 mm, b_2 = 2.4 mm, w_2 = 0.2 mm, b_3 = 2.16 mm, and w_4 = 0.09 mm.

Table 4. The elaborate geometrical parameters of the electric and magnetic meta-atoms utilized in region I and II.

$\mu_r = 1.807 + i0.057$ and $\varepsilon_z = 0.733 + i0.09$ for the first layer in region I and are $\mu_r = 1.441 + i0.032$ and $\varepsilon_z = 3.395 + i0.08$ for the 10th layer in region II. Due to small ε_z required in region I while large ε_z in region II, the working frequency is designed immediately above ω_p in region I while far away above ω_p in region II. In all cases, the imaginary parts of permittivity and permeability are found to be near zero while the real parts of them change slowly near 10 GHz, indicating a low loss and a relatively relaxed material dispersion. Moreover, the combined electric and magnetic resonators have lowered ω_p from 12 GHz (meta-atom without SRR) to 9.4 GHz, further facilitating electrically smaller particles which should advance a step toward the homogenization of bulk composites.

3.3. Numerical and experimental results

Now, we carry out full-wave simulations in COMSOL Multiphysics to demonstrate the functionality of proposed superscatterer illusion device. For comprehensive study and not lose generality, the superscatterer illusion for a dielectric object is also studied. As shown in **Figure 40**, a line source (a monopole probe in experiment) is located 50 mm (1.67 λ_0) away

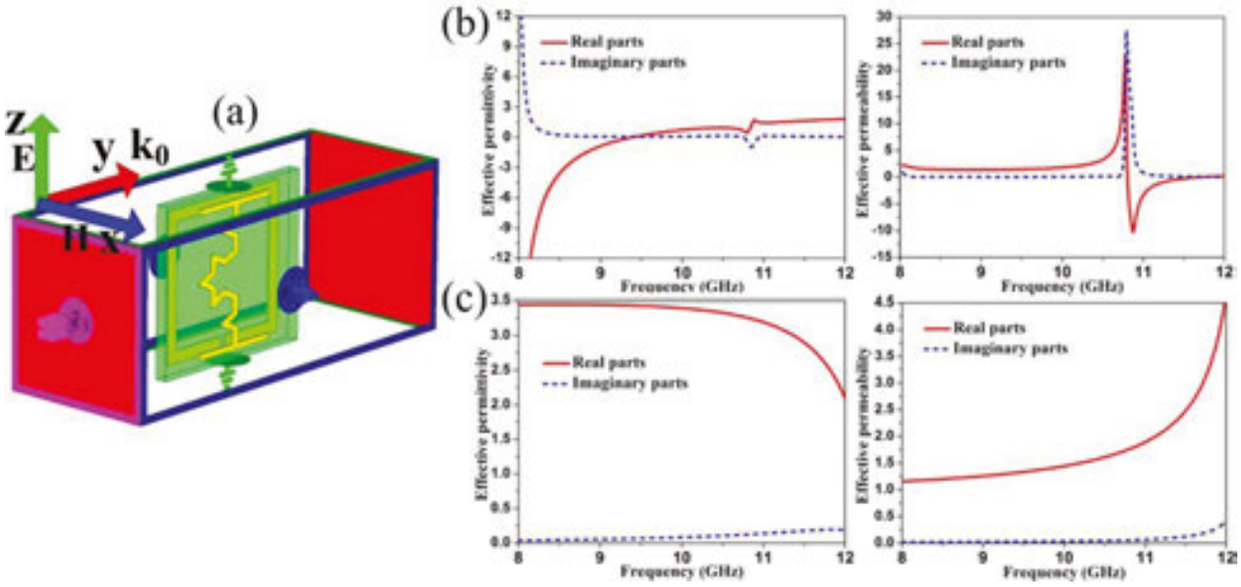

Figure 39. (a) Simulation setup for the meta-atom with periodic boundary conditions in HFSS. The retrieved constitutive parameters for (b) meta-atoms of the first layer in region I, and (c) those of the tenth layer in region II.

from the left edge of the illusion device in Case 1, whereas it is 57.5 mm (1.92 λ_0) in Case 2. Notice that the geometrical parameters of the devices in **Figure 40(a–d)** are exactly the same except for different number of wing objects. In all cases, the scattering patterns in actual and virtual spaces are in good consistency and equivalence, indicating that the superscatterer illusions are efficiently generated for both dielectric and metallic objects. Our device enables the camouflage of the radar image of a small cylinder to radar images of a large cylinder and two/four standalone objects. Moreover, the similar field patterns of the illusion devices with two and four wings indicate the robustness of the method in creating multiple isolated radar ghost images. Most importantly, the small signature of the original object is transformed to a larger one with arbitrary scaling ratios, enabling a superscatterer.

To further quantitatively evaluate the superscatterer illusion performance, we compare the simulation results of scattered electric fields in actual and virtual spaces within the region $-2\lambda_0 \le y \le 2\lambda_0$ at the rear side of the shell, see **Figure 41(a)**, where the field intensities along the line $x = 8.27\lambda_0$ in both spaces range from 0.014 to 0.182 V/m and have good consistency. As additional analysis, we also numerically discuss the sensitivity of the illusion performance to μ_r (real part) and loss (imaginary part of μ_r) along the line $x = 8.67\lambda_0$ in actual space. When it varies from μ_r to $\mu_r + i0.01\mu_r$ and finally to $\mu_r + i0.02\mu_r$, the wavefronts do not suffer substantial changes except for gradually decreased field intensities (e.g. the maximum values decrease from 0.158 to 0.131 V/m), see **Figure 41(b)**. Similarly, the scattered fields do not suffer significant change except for varied peak intensity when the real part of μ_r varies from μ_r to 1.25 μ_r, see **Figure 41(c)**. Therefore, the superscatterer illusion performance of our devices is insensitive to material loss and should exhibit a desirable operation bandwidth within the acceptable tolerances of material parameters.

http://dx.doi.org/10.5772/65603

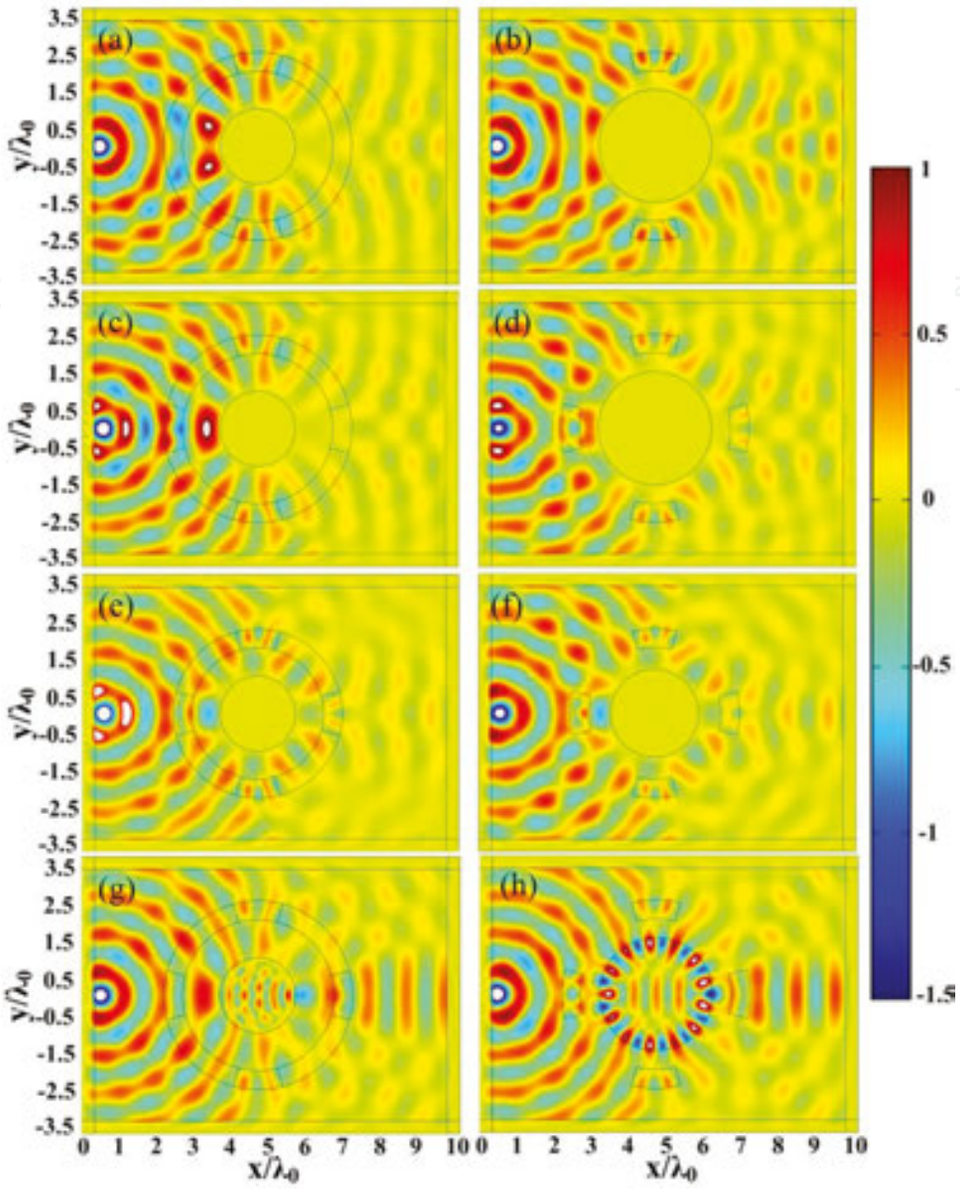

Figure 40. Simulated snapshots of electric-field distributions at 10 GHz in actual space (the left column) and virtual space (the right column). A metallic cylinder is wrapped by simplified-parameter illusion devices for (a) two and (c) four dielectric wings in Case 1, and (e) four dielectric wings in Case 2. An enlarged metallic cylinder with (b) two dielectric wings in Case 1, and four dielectric wings in (d) Case 1 and (f) Case 2. (g) A dielectric cylinder wrapped by an illusion device with four dielectric wings and simplified parameter in Case 1. (h) An enlarged dielectric cylinder with four dielectric wings in Case 1.

To validate the superscatterer illusion functionality, we measured 2D electric-field mappings in near-field parallel-plate waveguide measurement system (**Figure 42**). A monopole probe fixed inside the planar waveguide excites the sample over a discrete cluster of frequencies. The impinging EM wave interacts with thousands of particles and thus affords desired scattering signatures. Due to large size of the sample, the simulated and measured electric fields in horizontal plane are mainly recorded at rear side of the device ($7\lambda_0 \le x \le 10.2\lambda_0$ and $-2\lambda_0 \le y \le 2\lambda_0$) at 10.1, 10.15, 10.21, 10.25 and 10.3 GHz, respectively, see **Figure 43**.

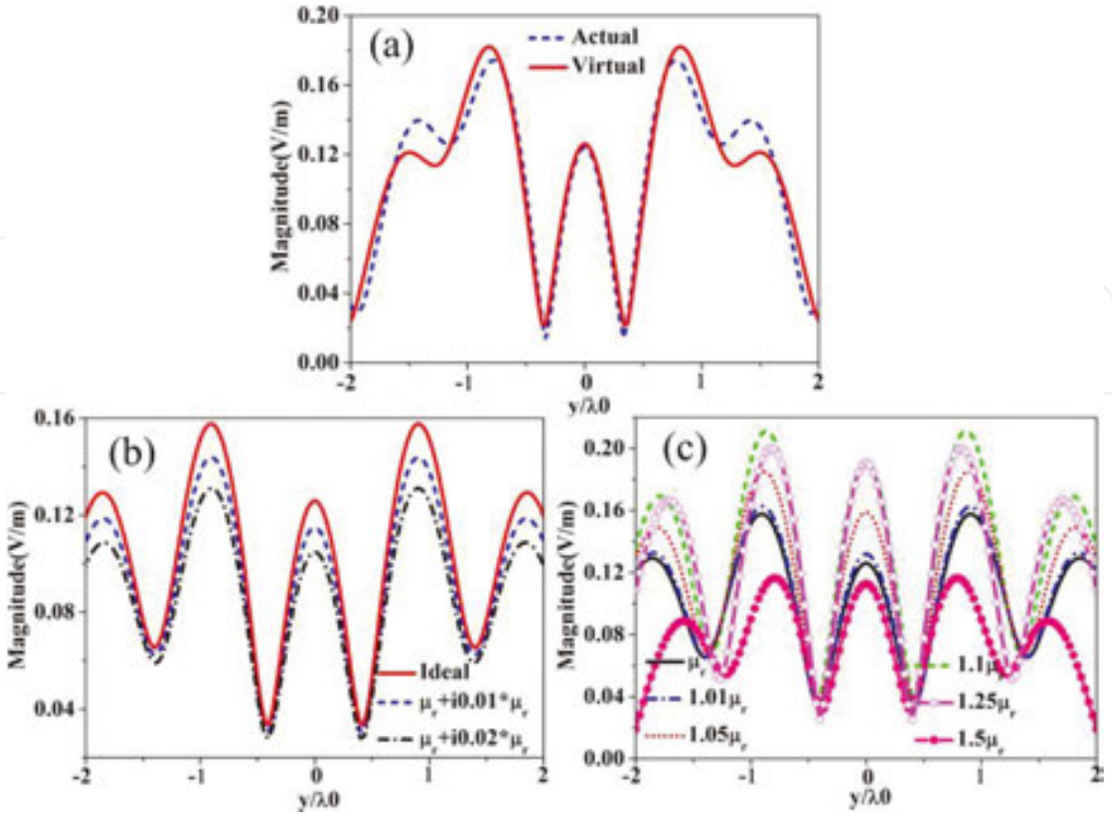

Figure 41. (a) Scattered electric fields in actual and virtual spaces along the line $x = 8.27\lambda_0$. Scattered electric fields in actual space along the line $x = 8.67\lambda_0$ for (b) different loss and (c) different real parts of μ_r.

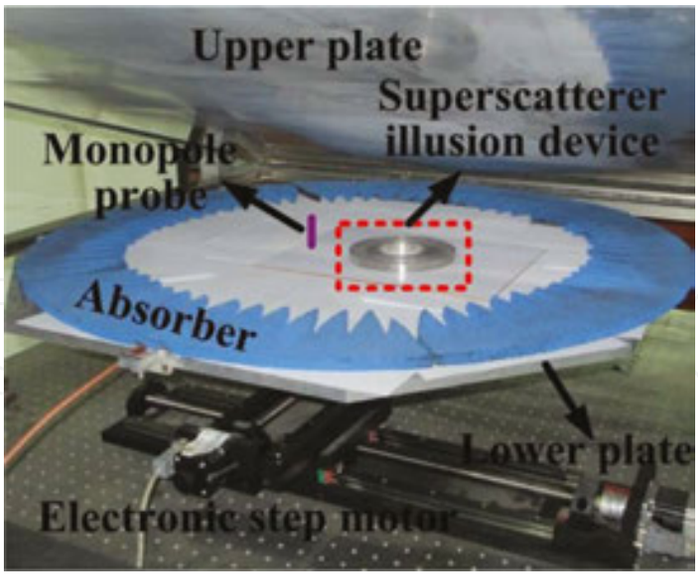

Figure 42. Experimental setup for 2D electric-field mapping in near-field parallel-plate waveguide measurement system.

As shown in **Figure 43(a)** and **(d)**, the simulated and measured scattering patterns are in reasonable agreement. The consistency can be further inspected from electric-field intensities shown in **Figure 43(g)**, where the fields at 10.1 GHz are normalized to the maximum along the black dashed line $x = 9.57\lambda_0$. In all simulated and measured cases shown in **Figure 43(a–f)**, the

http://dx.doi.org/10.5772/65603

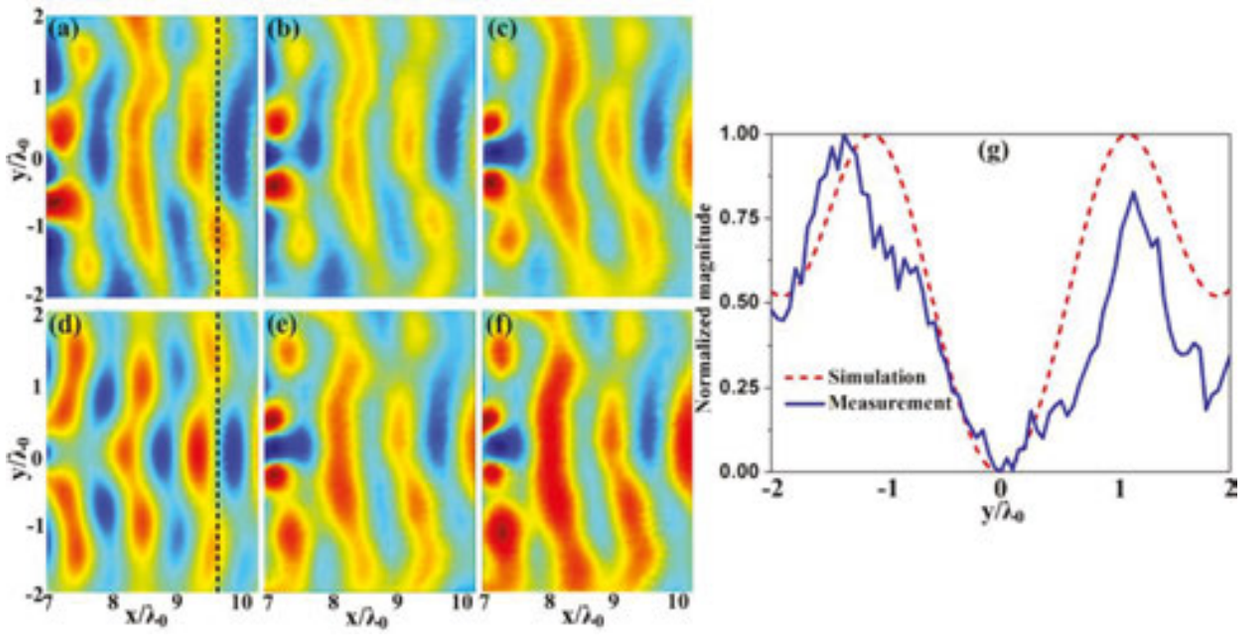

Figure 43. Comparison of simulated and measured electric-field distributions. (d) Simulated and (a–c, e, and f) measured results at (a and d) 10.1 GHz, (b) 10.15 GHz, (c) 10.21 GHz, (e) 10.25 GHz, and (f) 10.3 GHz. (g) Normalized electric-field intensity along the black dashed line $x = 9.57\lambda_0$.

uneven wavefronts with convex curves at both ends and concave curves in the interspace, along with a remarkable perturbation in the first outgoing wavefront from the illusion device are clearly observed, illustrating the effectiveness and robustness of the design. Hence, the superscatterer illusion functionality, i.e., the transformation of the radar signature of an object to the equivalence of an enlarged object and four isolate dielectric objects is unambiguously validated over a bandwidth of more than 200 MHz. The shifted operation frequency and slight distortion of electric fields in measurements are possibly attributable to the tolerance inherent in fabrications and assembling, the utilized adhesives to connect meta-atoms at the interfaces of different regions and the misalignment of particles along radial direction.

4. Conclusions

In summary, we have reviewed in this chapter our recent effort in synthesizing electrically small meta-atoms from effective medium perspective and utilizing compact meta-atoms to design microwave circuits and functional devices. Several strategies have been proposed for such a purpose and the mechanisms have been studied in depth. The advantages of compact meta-atoms can be classified in two categories. First, it can significantly reduce the circuit size without posing penalty on device performances. Second, it brings about additional degree of freedom for device design and broadband deep out-of-band signal inhibition which can be employed for harmonic suppression. Third, it enables manipulation of precise material parameters and smooth outgoing field which is preferable for functional devices with high performances and new physics demonstration with high-quality phenomena. Moreover, the precise-material parameters will improve the success rate of correct design. Our compact approach

lays a platform and gives a promising alternative for both engineers and scientists to realize their devices or demonstrate their find using metamaterials.

Acknowledgements

This work was supported by National Natural Science Foundation China under Grant Nos. 61501499 and 61372034 and also Natural Science Foundation of Shaanxi Province under Grant 2016JQ6001. The authors deliver their special gratitude to Prof. Tie Jun Cui and his meta-group for the guidance, discussions and help afforded in the work of 3D super lens and illusion device.

Author details

He-Xiu Xu*, Guang-Ming Wang, Tong Cai, Qing Peng and Ya Qiang Zhuang

*Address all correspondence to: hxxuellen@gmail.com

Microwave Laboratory, Air Force Engineering University, Changle, Xi'an, China

References

[1] Bahl I, "Lumped elements for RF and microwave circuits," Boston: Artech House, Ch. 14, 2003, pp. 462–465.

[2] E.-Y. Jung and H.-Y. Hwang, "A balun-BPF using a dual mode ring resonator," *IEEE Microw. Wireless Compon. Lett*., vol. 17, no. 9, pp. 652–654, Sep. 2007.

[3] Y.-X. Guo, K.-W. Khoo and L. C. Ong, "Wideband circularly polarized patch antenna using broadband baluns," *IEEE Trans. Antennas Propag*., vol. 56, no. 2, pp. 319–326, Feb. 2008.

[4] T.-G. Ma and Y.-T. Cheng, "A miniaturized multilayered Marchand balun using coupled artificial transmission lines," *IEEE Microw. Wireless Compon. Lett*., vol. 19, no. 7, pp. 446–448, Jul. 2009.

[5] Y.-X. Guo, Z. Y. Zhang, L. C. Ong and M. Y. W. Chia, "A novel LTCC miniaturized dualband balun," *IEEE Microw. Wireless Compon. Lett*., vol. 16, no. 3, pp. 143–145, Mar. 2006.

[6] C.-H. Tseng and Y.-C. Hsiao, "A new broadband Marchand balun using slot-coupled microstrip lines," *IEEE Microw. Wireless Compon. Lett*., vol. 20, no. 3, pp. 157–159, Mar. 2010.

[7] C.-H. Tseng and C.-L. Chang, "Wide-band balun using composite right/left-handed transmission line," *Electron. Lett*., vol. 43, no. 21, pp. 1154–1155, Oct. 2007.

[8] Z.-Y. Zhang and K.Wu, "A broadband substrate integrated waveguide planar balun," *IEEE Microw. Wireless Compon. Lett*., vol. 17, no. 12, pp. 843–845, Dec. 2007.

[9] J.-L. Li, S.-W. Qu and Q. Xue, "Miniaturised branch-line balun with bandwidth enhancement," *Electron. Lett*., vol. 43, no. 17, pp. 931–932, Aug. 2007.

[10] C. Liu and W. Menzel, "Broadband via-free microstrip balun using metamaterial transmission lines," *IEEE Microw. Wireless Compon. Lett*., vol. 18, no. 7, pp. 437–439, Jul. 2008.

[11] C.-C. Chen and C.-K. C. Tzuang, "Synthetic quasi-TEM meandered transmission lines for compacted microwave integrated circuits," *IEEE Trans. Microw. Theory Tech*., vol. 52, no. 6, pp. 1637–1647, Jun. 2004.

[12] H.-X. Xu, G.-M. Wang, X. Chen, et al. "Broadband balun using fully artificial fractal-shaped composite right/left handed transmission line," *IEEE Microw. Wireless Compon. Lett*., vol. 22, pp. 16–18, 2012.

[13] W. Shao, J. He and B.-Z. Wang, "Compact rat-race ring coupler with capacitor loading," *Microwave Opt. Technol. Lett*., vol. 52, no. 1, pp. 7–9, 2010.

[14] J. Wang, B.-Z. Wang, Y.-X. Guo, L. C. Ong and S. Xiao, "Compact slow-wave microstrip rat-race ring coupler," *Electron. Lett*., vol. 43, no. 2, pp. 111–113, 2007.

[15] J.-T. Kuo, J.-S. Wu and Y.-C. Chiou, "Miniaturized rat race coupler with suppression of spurious passband," *IEEE Microw. Wireless Compon. Lett*., vol. 17, no. 1, pp. 46–48, 2007.

[16] S. Opozda, P. Kurgan and M. Kitlinski, "A compact seven-section rat-race hybrid coupler incorporating PBG cells," *Microwave Opt. Technol. Lett*., vol. 51, no. 12, pp. 2910–2913, 2009.

[17] P. H. Rao, J. Subramanian and M. Kamki, "Miniaturized broadband microstrip fractal rat-race coupler with shunt stubs," *Microwave Opt. Technol. Lett*., vol. 52, no. 2, pp. 289–292, 2010.

[18] H. Ghali and T. A. Moselhy, "Miniaturized fractal rat-race, branch-line and coupled-line hybrids," *IEEE Trans Microwave Theory Tech*., vol. 52, no. 11, pp. 2513–2520, 2004.

[19] H. Ghali and T. Moselhy, "Design of fractal rat-race coupler," *IEEE MTT-S Int. Microwave Symp. Dig*., pp. 324–327, 2004.

[20] K.-K. M. Cheng and F.-L. Wong, "Dual-band rat-race coupler design using tri-section branch-line," *Electron. Lett*., vol. 43 no. 6, pp. 41–42, 2007.

[21] K.-S. Chin, K.-M. Lin, Y.-H. Wei, T.-H. Tseng and Y.-J. Yang, "Compact dual-band branch-line and rat-race couplers with stepped-impedance-stub lines," *IEEE Trans. Microwave Theory Tech*., vol. 58, no. 5, pp. 1213–1221, 2010.

[22] M. K. Mandal and S. Sanyal, "Compact dual-band rat-race couplers," *Microwave Opt. Technol. Lett*., vol. 50, no. 2, pp. 277–281, 2008.

[23] H.-X. Xu, G.-M. Wang, X.-K. Zhang, et al. "Novel compact dual-band rat-race coupler combining fractal geometry and CRLH TLs," *Wireless Pers. Commun*., vol. 66, no. 4, pp. 855–864, 2012.

[24] P.-L. Chi and T. Itoh, "Miniaturized dual-band directional couplers using composite right/left-handed transmission structures and their applications in beam pattern diversity systems," *IEEE Trans Microwave Theory Tech*., vol, 57, no. 5, pp. 1207–1215, May 2009.

[25] C. Caloz and T. Itoh, "Electromagnetic metamaterials: transmission line theory and microwave applications: the engineering approach ," Hoboken, New Jersey: Wiley-Interscience, 2006.

[26] H.-X. Xu, G.-M. Wang, C.-X. Zhang, Z.-W. Yu and X. Chen, "Composite right/left-handed transmission line based on complementary single-split ring resonator pair and compact power dividers application using fractal geometry," *IET Microw. Antennas Propag*., vol. 6, no. 9, pp. 1017–1025, 2012.

[27] H.-X. Xu, G.-M. Wang, Z.-M. Xu, et al. "Dual-shunt branch circuit and harmonic suppressed device application," *Appl. Phys. A*, vol. 108, no. 2, pp. 497–502, 2012.

[28] R. Marques, F. Martin and M. Sorolla. "Metamaterials with negative parameters: theory, design and microwave applications," Hoboken, NJ: Wiley, 2008.

[29] A. K. Iyer and G. V. Eleftheriades, "Volumetric layered transmission-line metamaterial exhibiting a negative refractive index," *J. Opt. Soc. Am. B*, vol. 23, pp. 553–570, 2006.

[30] A. K. Iyer and G. V. Eleftheriades. "A multilayer negative-refractive-index transmission-line (NRI-TL) metamaterial free-space lens at X-Band," *IEEE Trans. Antennas Propag*., vol. 55, pp. 2746–2753, 2007.

[31] H.-X. Xu, G.-M. Wang, M. Q. Qi, et al. "Three-dimensional super lens composed of fractal left-handed materials," *Adv. Opt. Mater*., vol. 1, no. 7, pp. 495–502, 2013.

[32] H.-X. Xu, G.-M. Wang, K. Ma and T. J. Cui, "Superscatterer illusions without using complementary media," *Adv. Opt. Mater*., vol. 2, no. 6, pp. 572–580, 2014.

[33] B. L. Zhang and G. Barbastathis, "Dielectric metamaterial magnifier creating a virtual color image with far-field subwavelength information," *Opt. Express*, vol. 18, p. 11216, 2010.

[34] W. X. Jiang, C.W. Qiu, T. C. Han, Q. Cheng, H. F. Ma, S. Zhuang and T. J. Cui, "Broadband all-dielectric magnifying lens for far-field high-resolution imaging," *Adv. Mater*., vol. 25, pp. 6963–6968, 2013.

[35] W. X. Jiang, C.-W. Qiu, T. Han, et al. "Creation of ghost illusions using wave dynamics in metamaterials," *Adv. Funct. Mater*., vol. 23, pp. 4028–4034, 2013.